2004-04-21

Fluorescence Detectors for Proteins and Toxic Heavy Metals

Uchenna Prince Paul
Brigham Young University - Provo

FLUORESCENCE DETECTORS FOR PROTEINS AND TOXIC METALS

by

Uchenna Prince Paul

A thesis submitted to the faculty of

Brigham Young University

in partial fulfillment of the requirements for the degree of

Master of Science

Department of Chemistry and Biochemistry

Brigham Young University

April 2004

BRIGHAM YOUNG UNIVERSITY

GRADUATE COMMITTEE APPROVAL

of a thesis submitted by

Uchenna Prince Paul

This thesis has been read by each member of the following graduate committee and by majority vote has been found to be satisfactory.

_____	_____
Date	Paul B. Farnsworth, Chair
_____	_____
Date	Matthew C. Asplund
_____	_____
Date	Matthew R. Linford
_____	_____
Date	Paul B. Savage

BRIGHAM YOUNG UNIVERSITY

As chair of the candidate's graduate committee, I have read the thesis of Uchenna Prince Paul in its final form and have found that (1) its format, citations, and bibliographical style are consistent and acceptable and fulfill university and department style requirements; (2) its illustrative materials including figures, tables, and charts are in place; (3) the final manuscript is satisfactory to the graduate committee and us ready for submission to the university library.

_____
Date

_____
Paul B. Farnsworth
Chair, Graduate Committee

Accepted for the Department

_____
Francis R. Nordmeyer
Department Chair

Accepted for the College

_____
Earl M. Woolley
Dean, College of Physical
and Mathematical Sciences

ABSTRACT

FLUORESCENCE DETECTORS FOR PROTEINS AND TOXIC METALS

Uchenna P. Paul

Department of Chemistry and Biochemistry

Master of Science

An inexpensive detector for proteins is described. The detection technique was based on two-photon excitation intrinsic protein fluorescence using a visible 532 nm diode-pumped nano laser as the excitation source. Proteins that exhibit intrinsic fluorescence must contain at least one tryptophan, tyrosine, or phenylalanine residue in their amino acid sequences. The detector was characterized and was found to have a detection limit of 4 μM for tryptophan, 22 μM for tyrosine and 500 μM for phenylalanine. Bovine serum albumin, a serum protein with 3 tryptophan residues in its amino acid sequence was also used to characterize the detector. It was found that the detection limit for this protein was 0.9 μM. The detector volume was determined based on a photon counting histogram – a technique in fluorescence fluctuation spectroscopy. From the results of this analysis, the excitation volume was found to be 2.9 fL. With such an excitation volume, the detection limits were either within or below the atto-mole range.

5-chloro-8-methoxyquinoline appended-diaza-18-crown-6 is a promising chemosensor for the detection of cadmium. The uncomplexed ligand is weakly fluorescent; but with cadmium, its fluorescent quantum yield and lifetime increase dramatically. The spectroscopic properties of immobilized 5-chloro-8-methoxyquinoline appended-diaza-18-crown-6 on a quartz substrate by coating with polymers were studied and were found to be similar to those in solution. An online field-usable cadmium sensor was then designed and fabricated that uses covalently bound 5-chloro-8-methoxyquinoline appended-diaza-18-crown-6 on quartz as the heart of the sensor.

ACKNOWLEDGMENTS

I wish to thank Paul B. Farnsworth for his mentoring and for the opportunity given to me to carry out this work.

My family has been very supportive and I would like to thank them and let them know that I am indebted to them for their encouragement, support and prayers.

I will not forget to thank Paul Savage, Matthew Asplund, and my friends for their support.

Lastly, I thank Heavenly Father for making this a dream come true

TABLE OF CONTENTS

Chapter 1

Introduction to Protein Detection

There has been growing interest in the detection and quantitation of proteins. In fact this growing interest has given rise to a new field called proteomics – the large scale screening of proteins of a cell, organism, or biological fluid [1]. In the human body, disease biomarkers are expressed mostly as proteins; recent improvement in survival rate of patients with early disease diagnosis underscores the need for protein detection [2].

Various forms of detection techniques have been applied to protein detection. These include electrochemical detection, mass spectrometry, radioactive isotopic techniques, optical techniques, etc. M. Masarik *et al.* used square-wave voltammetry in combination with an adsorptive transfer stripping technique to measure nanogram quantities of streptavidin and avidin in solution by measuring the oxidative signals of tryptophan and tyrosine residues in the protein [3]. Mass spectrometry as a technique for the detection of proteins became popular following the discovery of matrix assisted laser desorption ionization (MALDI) and electrospray ionization (ESI) as soft ionization techniques for macromolecules such as proteins and peptides. Mass spectrometry is widely used especially in protein sequencing. However, it requires expensive equipment and highly skilled personnel.

Optical detection, which includes absorption, scattering and luminescent methods has also been used to detect proteins. Among the optical methods, luminescent methods give the lowest detection limits. The most commonly employed luminescent technique is

laser induced fluorescence (LIF). Its sensitivity is several orders of magnitude higher than absorption or scattering methods [4].

1.1 Protein Detection with LIF

Protein detection with LIF can be either by native (intrinsic) fluorescence or by fluorescence due to a label or tag (fluorophore) on the protein. Though impressive detection limits have been reported with labeling [5], there exist inherent problems with this approach, such as complicated sample preparation and handling and multiple reaction products from a single protein, that complicates separation techniques [1, 4]. Because of these problems, many research groups have focused on optical detection of proteins based on the protein's intrinsic fluorescence [6 – 7]. Proteins that do exhibit intrinsic fluorescence must contain tryptophan, tyrosine, or phenylalanine residues. Most proteins contain at least one tryptophan residue. However, it is not uncommon to find proteins with about 1.1 mol % tryptophan. The use of tryptophan fluorescence has not just been limited to the detection and quantitation of proteins alone; rather it has also been used to study the dynamic nature of proteins such as folding and denaturation, protein-protein interactions, tissue engineering and developmental biology [8 – 9].

1.1.1 Spectral Properties of Tryptophan, Tyrosine, and Phenylalanine

As stated in the preceding paragraph, protein fluorescence is usually from the aromatic amino acids. These aromatic amino acids exhibit strong UV absorption with peaks at 258 nm for phenylalanine; 275 nm for tyrosine; and 278 nm for tryptophan [10]. Figure 1–1 shows the excitation and emission spectra of tryptophan, tyrosine, and phenylalanine in water respectively [11]. From the figure, it can be observed that

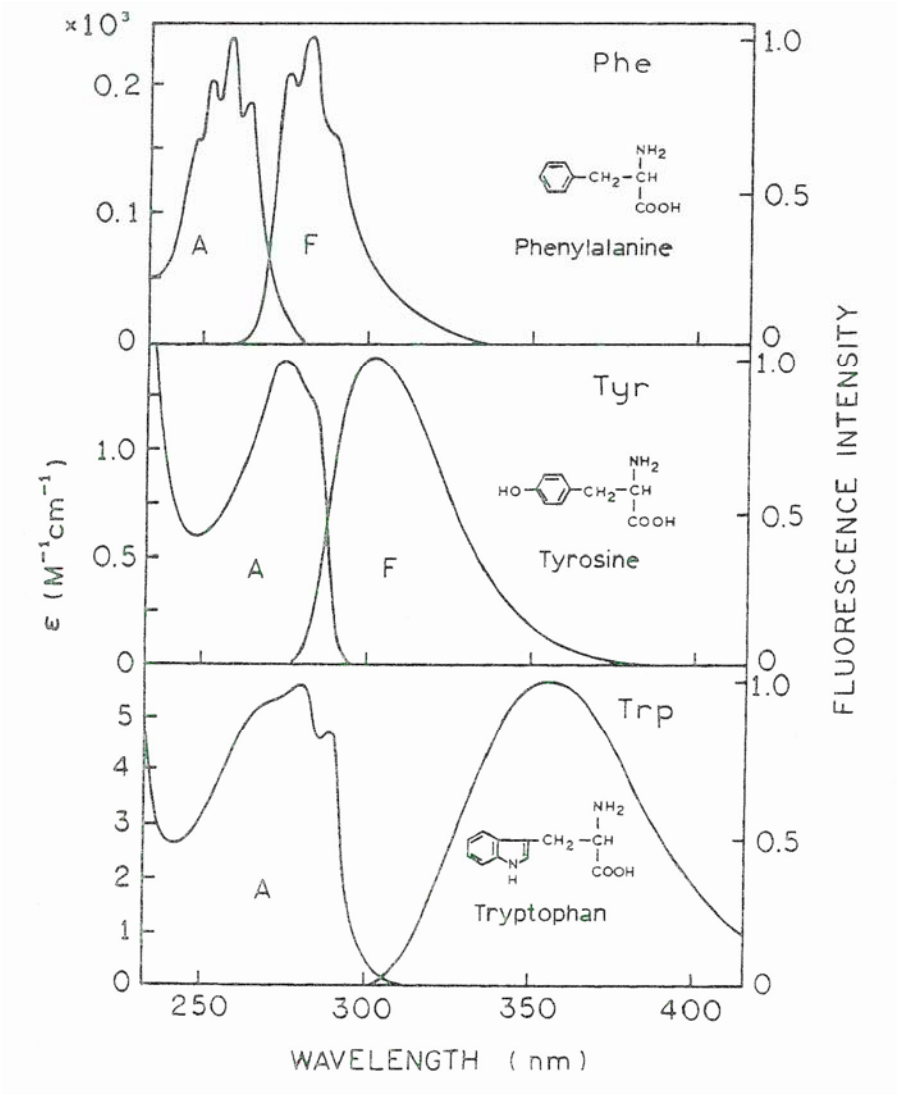

Figure 1-1 Excitation and emission spectra of aqueous solutions of the aromatic amino acids tryptophan, tyrosine, and phenylalanine respectively [11].

the emission maxima for these amino acids are 350 nm for tryptophan, 303 nm for tyrosine, and 282 nm for phenylalanine. Amongst these three aromatic amino acids, tryptophan has the highest quantum yield (0.2) followed by tyrosine (0.14) and phenylalanine (0.04). Please note that these values are in water [12].

The electronic spectrum of the indole ring in tryptophan is responsible for its absorption while the phenol ring in tyrosine and the benzene ring in phenylalanine are responsible for their absorptions respectively. In solution, it has been shown that both indole and phenol have two absorption bands in the UV both of which are $\pi^* \leftarrow \pi$ singlet – singlet transitions [13 – 14]. In both cases, the two excited states are labeled ^1L_a and ^1L_b under Platt's notation [15]. The lowest singlet energy transition of tyrosine is due to the ^1L_b band, which has a maximum 275 nm. The ^1L_a band has a maximum around 223 nm. Figure 1–2a shows the singlet – singlet electronic absorption transition moments of phenol ring in tyrosine while Figure 1–2b shows the Jablonsky energy level diagram for the phenol ring. In the gas phase, the ^1L_b state of the indole is also lower in energy than the ^1L_a state and are separated by about 1400 cm^{-1} [16]. When indole interacts with polar solvents, the ^1L_a state could become lower in energy than the ^1L_b state due to the solvent's interaction with the π cloud [14, 16].

Consequently the spectral properties of these acids are strongly dependent on pH and other environmental factors such as solvent polarity and temperature [17]. Both the quantum yields and emission maxima are affected by pH. At a pH range of 4.0 – 9.0, a maximum is observed for the fluorescence quantum yields of these amino acids [10].

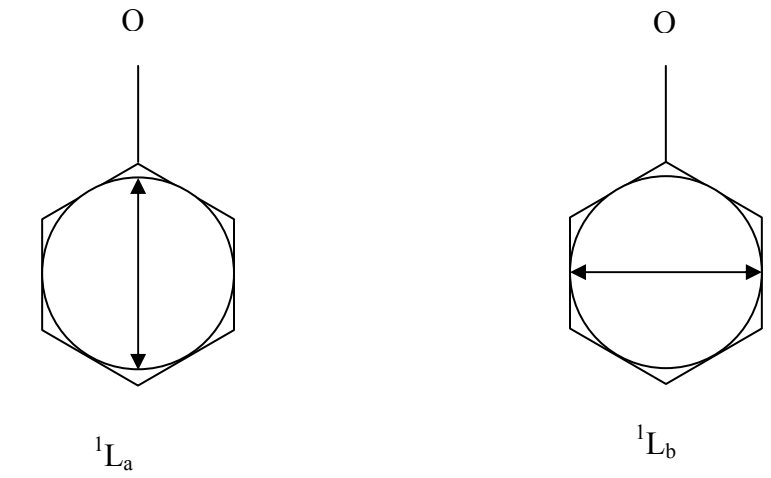

(A)

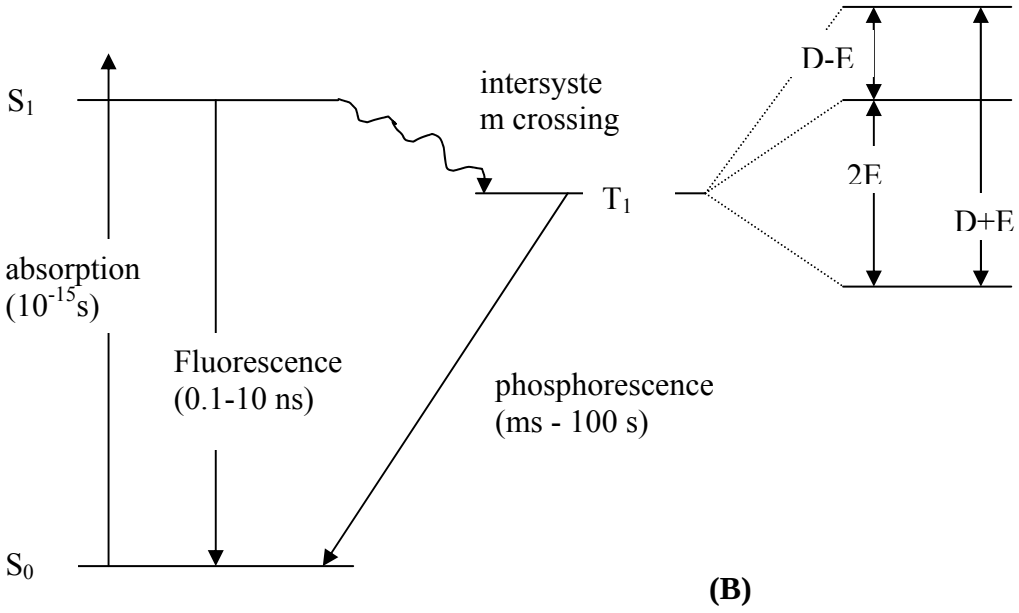

(B)

Figure 1–2. (A) Singlet – singlet electronic absorption transition moment orientations of phenol ring in tyrosine. (B) Jablosnski energy level diagram showing the singlet state and the triplet state with its zero-field splittings for a planar aromatic chromophore [13].

In principle, the emission of proteins containing the three aromatic amino acids should be the summation of the respective emissions from these amino acids. However, the observed emission is seldom the case. It has been shown that there is significant resonance energy transfer from phenylalanine to tyrosine and from tyrosine to tryptophan. This therefore makes observed protein emission to be essentially that of tryptophan. Similarly, in multi tryptophan containing proteins, it is difficult to separate the spectral contributions of each tryptophan residue in the protein. Tryptophan emission in proteins is also environmentally dependent. Depending on the environment, the emission maxima of tryptophan in proteins could range from 308 to 355 nm, while the quantum yields could vary from 0.4 to immeasurably low [18].

Similarly, tyrosine emission is significantly quenched if, in the protein molecule, it is exposed to a hydrated carbonyl group or a disulfide group or by hydrogen bonding with a peptide. Also, exposure of tyrosine buried in a peptide to ionized carboxyls will quench its emission and minimize its contribution to the total protein's fluorescence.

1.2 Practical Challenges of Intrinsic Protein Fluorescence

From previous sections, it was stated that the aromatic amino acids in proteins are responsible for their absorption (with exception of sulfur-sulfur peptide linkages) and emission and that they absorb and emit in the ultraviolet. This strong UV absorption presents practical challenges such as finding efficient and economical excitation sources, and discriminating against high absorption and emission from the background. Similarly,

tryptophan (the amino acid with the highest quantum yield) exhibits limited photostability [19].

To circumvent the enumerated problems above due to the conventional single-photon excitation (SPE) of these aromatic amino acid residues in proteins, many research groups have focused on two-photon excitation (TPE).

The goal of this project was to build a compact and inexpensive TPE-based detector for proteins that can easily be coupled to a microchip electromobility focusing (μ-EMF) separation device for the separation and concentration of proteins. The μ-EMF separation device is presently being developed by other research groups in the department of chemistry and biochemistry here at Brigham Young University.

1.3 Basic theory of TPE fluorescence

The conventional way of doing fluorescence spectroscopy requires that the molecule absorbs a photon whose energy is equal to the energy required for the molecule to undergo a transition from one real lower electronic state to an upper state. The molecule then relaxes through a radiative pathway emitting a photon whose energy is *stokes-shifted* from the absorbed energy. However, in the TPE process, the molecule absorbs two photons (successively or simultaneously) whose individual energies are less than that required for the transition in SPE to take place but whose sum of energies must be equal to that required for an SPE transition. When the absorbed two photons are of different energies, *Lakowicz* called it two-color two-photon excitation [20]. This concept is illustrated in figure 1 – 3.

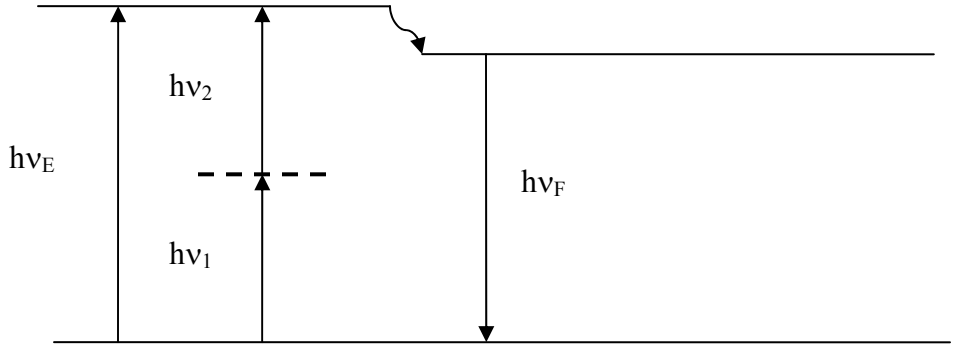

Figure 1-3. Energy diagram illustrating single-photon excitation (SPE) and two-photon excitation (TPE) and emission. In the first case, the molecule absorbs a photon whose energy is equal to $h\nu_E$ and becomes excited to the upper level. The molecule then relaxes to the ground state through a radiative path emitting a photon of energy $h\nu_F$. In TPE, the molecule first absorbs a photon whose energy is equal to $h\nu_1$. This energy is less than that required to excite the molecule to the upper state but can excite it to a virtual state of very short lifetime. If the lifetime is long enough for the molecule to absorb a second photon of energy $h\nu_2$ such that $h\nu_1 + h\nu_2 = h\nu_E$ then the molecule will be excited to the upper state and would then follow the same radiative pathway as in SPE and emit a photon of energy $h\nu_F$. Please note that $h\nu_1$ must not equal $h\nu_2$ rather $h\nu_1 + h\nu_2$ must be equal to $h\nu_E$. Here h and ν assume their usual meanings of plank constant and frequency.

In TPE, the molecule is first excited to a virtual state upon the absorption of the first photon. The lifetime of this virtual state is very short (within 10^{-15} – 10^{-16} s) [21] as a consequence of the Heisenberg's uncertainty principle [22]. If within this lifetime the molecule absorbs another photon whose energy is equal to that between the virtual state and the real upper state, then TPE occurs and the molecule can relax through a radiative pathway emitting a photon. Therefore to have TPE, very high photon fluxes are required (in the excess of 10^5 W/cm^2) [23]. Furthermore, the transition probability depends on how close the energy of the first absorbed photon is to the energy of a real excited state. The closer it is, the higher the transition probability. Similarly, it is interesting to state here that both SPE and TPE emission spectra are the same.

Usually in SPE, the amount of radiation absorbed is proportional to the intensity of the excitation radiation according to Beer's law. However in TPE, the consequence of simultaneous absorption of two photons leads to a quadratic dependence of the emission intensity on the excitation intensity according to the equation:

$$P_{2h\nu}(t,\lambda) = KC\delta\frac{l}{A}P^2(t,\lambda)\left[\frac{\Phi}{2}\right] \qquad (1-1)$$

Where $P_{2h\nu}(t,\lambda)$ is the measured fluorescence as a function of time and wavelength in (photons/s) emitted due to TPE and $P(t,\lambda)$ is the instantaneous power of the excitation source. K, C, δ, l and A are collection efficiency; sample concentration; two-photon absorption cross-section; path length; and area respectively. Φ is the quantum yield.

One implication of this quadratic dependence of the emission on the excitation intensity is that for a tightly focused beam, because the intensity is highest at the focal point, excitation events are only limited to the focal point. This makes TPE very good for microscopy and depth profiling. Similarly there is a reduction in photobleaching and photo-toxicity making TPE microscopy advantageous for live cells and tissues [25]. Nevertheless, TPE is not very sensitive because of the small absorption cross-sections which are typically in the order of 10^{-50} cm^4s/(photon molecule). This poor sensitivity has limited the application of TPE.

1.4 Basic Instrumentation of a TPE

As indicated above, TPE requires a very high photon flux. Hence researchers have mostly used mode-locked high repetition rate femtosecond pulsed lasers as the excitation source [22, 26]. A high power picosecond cavity-dumped dye laser that is synchronously pumped with a mode locked frequency doubled Nd:YAG laser has also been used [27 – 28]. Similarly *Yeung et al* [29] demonstrated TPE on oxadiazoles using very high power continuous wave argon ion laser. A mode-locked argon ion pumped pyridine-2 dye laser of pulse width near 7 ps has also been used to accomplish two-color two-photon excitation of indole [20]. In this case the fundamental (780 nm) and the frequency doubled (380 nm) outputs of the dye laser were overlapped. For most applications, the laser is usually focused tightly onto the sample using a microscope objective. The same objective can be used to collect the emission [30 – 31].

Because of long *blue-shift* between the excitation source wavelength and the emission wavelength, there is ease in the choice of filters that can be used to remove source scatter and specular reflections. Similarly, materials for the sample container do not have to be transparent at the uv excitation wavelength for the analytes.

Figure 1-4 shows the basic optical diagram of a conventional TPE setup on an epi illumination configuration. In this setup, light from the laser is focused tightly onto the sample using a high numerical aperture microscope objective. The same objective is used to collect the emission which is reflected off the dichroic mirror to the photomultiplier tube.

Other configurations of TPE have been reported including TPE excitation by the evanescent wave from total internal reflection [32] and in planer waveguides [23]. In both cases, femtosecond pulse Ti:Sapphire lasers were used as the excitation sources.

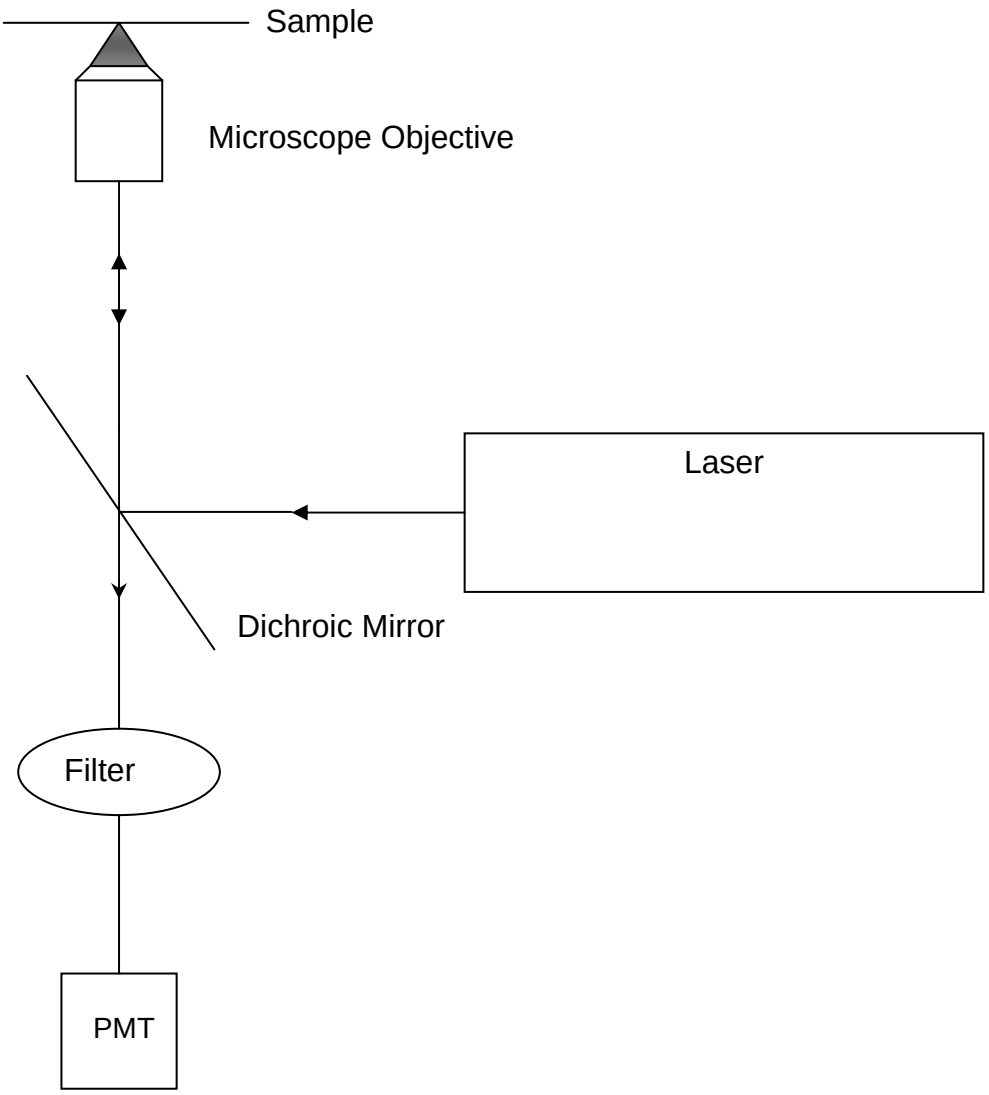

Figure 1-4. Typical epi illumination TPE setup. Light from the laser source is focused unto the sample with a high numerical aperture microscope objective. The same objective is used to collect the fluorescence and transmitted through the dichroic mirror; filtered and then detected by the PMT or an avalanche photodiodes.

1.5 Overview of Previous Studies

There has been a considerable amount of research on TPE detection of proteins and microscopy of cells and cellular materials [34]. In fact there exist commercially available TPE microscopes for protein imaging. Such microscopes are however very expensive. TPE has been applied to capillary electrophoresis of peptides [7] and catecholamines [35]. *Shear et. al*. [7] reported a detection limit of 0.3 μM for tryptophan when their TPE instrument was coupled to capillary electrophoresis. TPE has also been utilized to detect single DNA fragments after labeling with a dye [36]. Single protein molecule detection was recently reported by using a model protein – hemocyanin from the tarantula *Eurypelma californicum* [19]. This particular *heme* protein contains 148 tryptophan residues in its amino acid sequence. Because of the varying composition of tryptophan in different proteins, detection limits of TPE protein detectors is usually reported in terms of the detector's detection limit for tryptophan.

The detectors already reported have mostly used very expensive femtosecond pulse Ti:Sapphire lasers as the excitation sources. CrLiASGAF and CrLiSAF have also been used [34]. These laser systems are not only very expensive but are very bulky as well. Though in principle these detectors could be coupled to a microchip separation device, however, their bulkiness defeats the usefulness and benefits of miniaturization.

1.6 Summary

Detection of proteins is in no doubt of great importance especially in disease diagnosis. Different types of detection methods and techniques have been utilized to detect proteins. Amongst these techniques, laser induced fluorescence offers very high sensitivity comparable to mass spectrometry. One approach to accomplish laser induced fluorescence is to tag the proteins with a known fluorophore that absorbs and also fluoresces in the visible. However, tagging has limitations such as complicated sample preparation and handling, multiple reaction products from a single protein, and when integrated into a separation system, could distort the mode of separation, leading to loss of resolution.

To circumvent the problems associated with protein tagging, native fluorescence from the proteins has been used. Proteins that fluoresce intrinsically must contain any of the aromatic amino acids – tryptophan, tyrosine, and phenylalanine. These aromatic amino acids absorb strongly in the ultraviolet and also emit in the ultraviolet. The strong uv absorption imposes serious practical challenges when doing conventional fluorescence measurements, such as difficulty in finding powerful and economical excitation sources and high background absorption and emission at these wavelengths.

Two-photon excitation which involves the simultaneous absorption of two individual photons by a molecule has been employed to minimize the problems associated with the conventional approach of measuring intrinsic fluorescence of proteins. This technique

requires high peak laser powers and has been shown to offer detection limits similar to those with labeled proteins but devoid of the problems associated with protein labeling.

Most of two-photon protein detectors are built with non-turnkey, very expensive and bulky laser systems. Such systems could be coupled to a microchip separation device, but due to their bulkiness and cost, such a coupling would defeat the object of miniaturization.

The work presented in this thesis demonstrates the feasibility of a compact and inexpensive protein detector that can be easily coupled to a microchip separation system, such as an electromobility focusing device, without defeating the objectives of miniaturization.

1.7 References

1. C. Sluszny and E. Yeung, One-*and two-dimensional miniaturized electrophoresis of proteins with native fluorescence detection* Anal. Chem. **76** (2004) 1357 – 1365.
2. H. Issaq, T. Conrads, D. Prieto, R. Tirumalai and T. Veenstra *SELDI-TOF MS for diagnostic proteomics* Anal. Chem. **75** (2003) 149A – 155A.
3. M. Masarik, R. Kizek, K. Kramer, S. Billova, M. Brazdova, J. Vacek, M. Bailey, F. Jelen and J, Howard, *Application of avidin-biotin technology and adsorptive transfer stripping square-wave voltammetry for detection of DNA hybridization and avidin in transgenic avidin maize*, Anal. Chem., **75** (2003) 2665 – 2669.
4. "Detection of the total-protein profile in gels, on blots and in capillary electrophoresis" *Molecular Probes*.
   http://www.probes.com/handbook/sections/0903.html
   [Accessed February 9, 2004]
5. H. Lee, D. Pinto, E. Arriaga, Z. Zhang and N. Dovidhi *Picomolar analysis of proteins using electrophoretically mediated microanalysis and capillary electrophoresis with laser-induced fluorescence detection*, Anal. Chem., **70** (1998) 4546 – 4548.
6. H. Chang and E. Yeung *On-column digestion of protein for peptide mapping by capillary zone electrophoresis with laser-induced native fluorescence detection* Anal. Chem. **65** (1993) 2947 – 2951

7. E. Okerberg and J. Shear *Attomole-level protein fingerprinting based on intrinsic peptide fluorescence* Anal. Chem. **73** (2001) 1610 – 1613
8. C. Pokalsky, P. Wick, E. Harmas, F. Lytle and R. Van Erren *Fluorescence resolution of the intrinsic tryptophan residues of bovine protein tyrosyl phosphatase* J. Biol. Chem. **270** (1995) 3809 – 3815.
9. Y. Chen and A. Periasamy *Characterization of two-photon excitation fluorescence lifetime imaging microscopy for protein localization* Microsc. Res. Tech. **63** (2004) 72 – 80.
10. T. Truong, R. Bersohn, P. Brumer, C. Luk and T. Tao *Effect of pH on the phosphorescence of tryptophan, tyrosine, and proteins* J. Biol. Chem. **242** (1967) 2979 – 2985.
11. J. Lakowicz *Principles of fluorescence spectroscopy*. Kluwer Academic/Plenum Publishers 2nd ed. (1999) 445 – 486.
12. "Intrinsic fluorescence of proteins and peptides" University of Hawaii. http://core.biotech.hawaii.edu/fluor.htm [Accessed 18 February, 2004]
13. .J. Lakowicz *Topics in fluorescence spectroscopy* Plenum Press **3**:Biochemical Applications (1992) 1 – 66.
14. G. Berden, W. Meerts and E. Jalviste *Rotationally resolved ultraviolet spectroscopy of indole, indazole, and benzimudazole: Inertial axis reorientation in the $S_1(^1L_b) \leftarrow S_0$ transitions* J. Chem. Phys. **103** (1995) 9596 – 9606.
15. J. Platt *Classification of spectra of cata-condensed hydrocarbons* J. Phys. Chem. **17** (1949) 484 – 495.

16. J. Carney, F. Hagemeister and T. Zwier The hydrogen-bonding topoplogies of indole-(water)n clusters from resonant ion-dip infrared spectroscopy J. Chem. Phys. **108** (1998) 3379 – 3382.

17. E. Kirby and R. Steiner *The influence of solvent and temperature upon the fluorescence of indole derivatives* J. Physc. Chem. **74** (1970) 4480 – 4490.

18. Y. Reshetnyak and E. Burstein *Decomposition of protein tryptophan fluorescence spectra into log-normal components. II. The statistical proof of discreteness if tryptophan classes in proteins* Biophys. J. **81** (2001) 1710 – 1734.

19. M. Lippitz, W. Erker, H. Decker, V. Holde and T. Basche *Two-photon excitation microscopy of tryptophan containing proteins* Proc. Natl. Acad. Sci. USA **99** (2002) 2772 – 2777.

20. I. Gryczynski, H. Malak, and J. Lakowicz *Two-color two-photon excitation of indole* Biospectroscopy **3** (1997) 97 – 101.

21. J. Lakowicz *Principles of fluorescence spectroscopy*. Kluwer Academic/Plenum Publishers **2nd ed.** (1999) 57 – 59.

22. J. Shear *Multiphoton-excited fluorescence in bioanalytical chemistry* Anal. Chem. **71** (1999) 598A – 605A.

23. G. Duveneck, M. Bopp, M. Ehrat, L. Balet, M. Haiml, U. Keller, G. Marowsky, and S. Soria *Two-photon fluorescence excitation of macroscopic areas on planar waveguides* Biosensors and Bioelectronics **18** (2003) 503 – 510.

24. W. Fisher, E. Wachter, F. Lytle, M. Armas and C. Seaton *Source-corrected two-photon excited fluorescence measurements between 700 and 880 nm* Appl. Spectrosc. **52** (1998) 536 – 545.

25. "Two-photon excitation fluorescence microscopy" Cell and developmental biology UNC School of medicine http://www-cellbio.med.unc.edu/facilities/tpm.htm. [Accessed 16 February, 2004]
26. M. Krikunova, A. Kummrow, V. Voigt, M. Rini, H. Lokstein, A. Moskalenko, H. Scheer, A. Razjivin, and D. Leupold *Fluorescence of native and carotenoid-depleted LH2 from chromatium minutissimum, originating from simultaneous two-photon absorption in the spectral range of the presumed (optical 'dark') S_1 state carotenoids* FEBS lett. **528** (2002) 227 – 229.
27. K. Overway and F. Lytle *Two-photon excitation profiles in cylindrical capillaries* Appl. Spectros. **52** (1998) 928 –
28. S. Zugel and F. Lytle *Two-photon excitation in square and cylindrical capillaries* Appl. Spectros. **54** (2000) 1203 – 1207.
29. M. Sepaniak and E. Yeung *Laser two-photon excited fluorescence detection for high pressure liquid chromatography* Anal. Chem **49** (1977) 1554 – 1556.
30. P. Dittrich and P. Schwille *Spatial two-photon fluorescence cross-correlation spectroscopy for controlling molecular transport in microfluidic structures Anal.* Chem. **74** (2002) 4472 – 4479.
31. G. Chirico, C. Fumagalli and G. Baldini *Trapped Brownian motion in single-and two-photon excitation fluorescence correlation experiments* J. Phys. Chem. B **106** (2002) 2508 – 2519.

32. I. Gryczynski, Z. Gryczynski, and J. Lakowicz *Two-photon excitation by the evanescent wave from total internal reflection Anal*. Biochem. **247** (1997) 69 – 76.

33. A. Majewska, G. Yiu, and R. Yuste *A custom-made two-photon microscope ad deconvolution system* Pflugers Arch-Eur J Physiol **441** (2000) 398 – 408.

34. M. Gostkowski, and J. Shear *Subattomole fluorescence determination of catecholamines in capillary electrophoresis effluent streams* J. Am. Chem. Soc. **120** (1998) 12966 – 12967.

35. A. Orden, H. Cai, P. Goodwin, and R. Keller *Efficient detection of single DNA fragments in flowing sample streams by two-photon fluorescence excitation* Anal. Chem. **71** (1999) 2108 – 2116.

Chapter 2

Instrument Design, Setup and Characterization

2.1 Introduction

As stated in the previous chapter, a TPE detector requires photon fluxes in the excess of 10^5 W/cm^2 [1]. Therefore, a short-pulse, high-repetition-rate laser and good tight focusing optics are the major components of an efficient TPE detector. In fact the laser source is the most important and expensive part of a TPE detector. The most commonly-used laser source for TPE is a mode-locked, high-repetition-rate (usually in the megahertz range), femtosecond-pulse Ti:Sapphire laser [2]. However, such laser systems are bulky and expensive (about $100,000) [3].

The TPE detector described in this chapter was built with a miniature and inexpensive laser system, thus making the entire detector system very compact (when compared to similar detectors described by other researchers). It is also easily adaptable to a microchip separation device without defeating the object of miniaturization. See figure 2–1. Detailed descriptions of the optical, data acquisition and signal processing designs and assembly will be presented in subsequent paragraphs. Also described in this chapter are the results of the various experiments carried out to characterize the performance of the TPE detector.

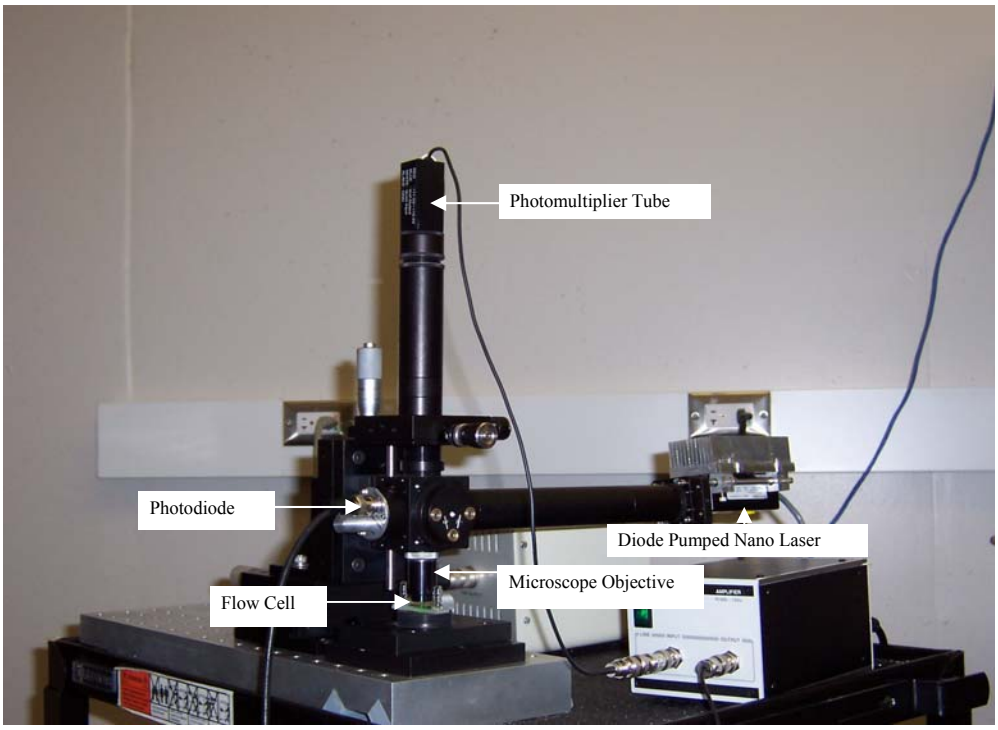

Figure 2-1. Picture of the two-photon excited fluorescence detector for proteins. This picture excludes some of the electronics used in the data acquisition and signal processing.

2.2 Optical setup

The optical setup consisted of the laser source, beam expander, dichroic mirror, microscope objective, emission focusing lens (tube lens), optical filter and a spatial filter. Figure 2-2 shows the diagram of the optical setup. The entire setup was mounted on an *x*-*y*-*z* translation stage.

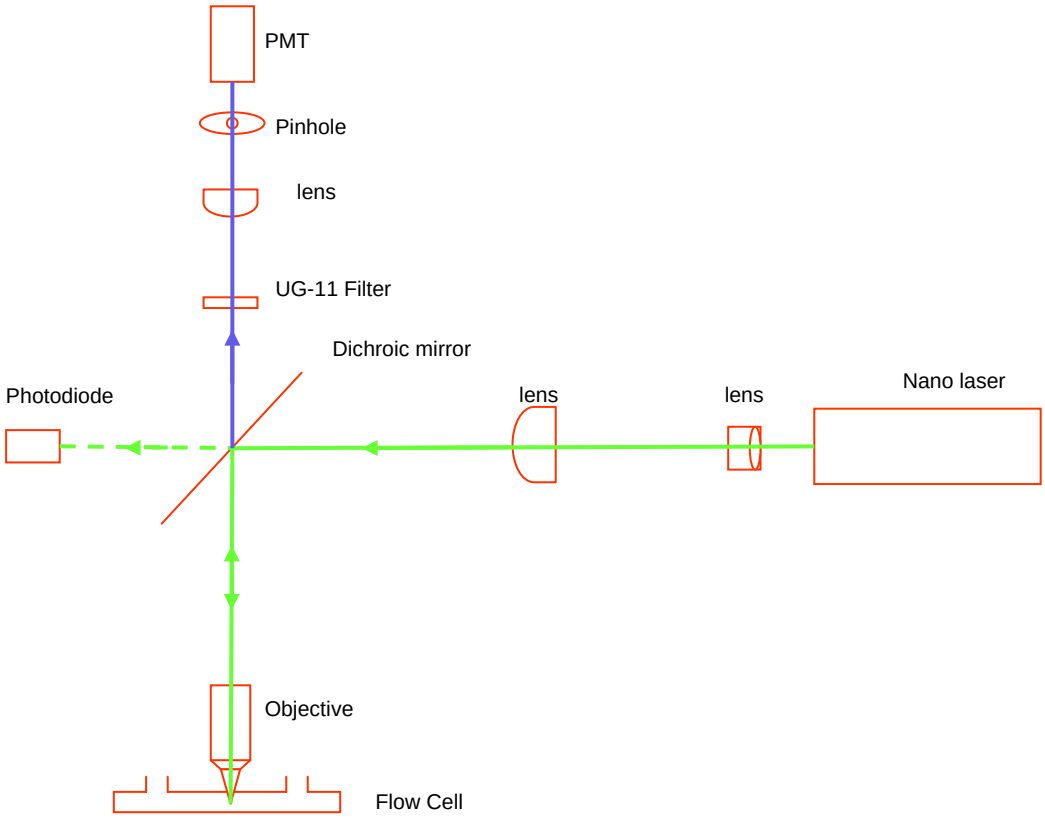

Figure 2-2 Optical setup of the two-photon detector. Light from the nano laser was expanded by the beam expander (accomplished by the two lenses following the laser), the expanded beam was reflected with the dichroic mirror to the microscope objective, which tightly focused the light unto the sample in the flow cell. Fluorescence from the sample was collected with the same objective and transmitted through the dichroic mirror after which the excitation scatter was removed by the UG11 filter. The emission was then focused to a pinhole for spatial filtering and the photomultiplier tube was used as a transducer for the optical signal to an electrical signal. Weakly transmitted excitation light through the dichroic mirror was detected by the photodiode, which was used as a trigger source for the data acquisition devices.

2.2.1 The Laser Source

The laser source used in the setup was a JDS Uniphase diode-pumped nano laser with laser head dimensions 100 mm x 22.4 mm x 22 mm. The laser emission wavelength was 532 nm with an average power of 29.3 mW; pulse width of 500 ps; repetition rate of 6.56 kHz; and a peak power of 8.9 kW. It was Q-switched with a saturable absorber and was mode-locked The natural laser line width of Nd:YAG is approximately 3 x 10^{12} Hz, corresponding a pulse width of 0.3 ps [4]. The transverse mode was TEM_{00} with a beam waist ($1/e^2$ radius) of 60 μm occurring 10 mm outside the laser head, and a beam divergence of ± 2 mrad. This high divergence of the laser beam was in accordance with the inverse relationship predicted by diffraction theory between the beam waist and the divergence angle in radians [5] according to the equation:

$$\theta = \frac{\lambda}{\pi\omega_0} \qquad (2-1)$$

where θ is the beam divergence in radians; λ is the wavelength of the laser beam and ω_0 is the beam waist. The exit beam diameter was 0.2 mm. The choice for this laser was not guided alone by the fact that it was compact and inexpensive, but also that it could deliver a peak power of 8.9 kW, which when focused to a spot of about 3 μm would lead to an irradiance of 3.1 x 10^{10} W/cm^2 (assuming no losses). This irradiance was more than 1 x 10^5 W/cm^2 minimum irradiance required to obtain TPE [6].

2.2.2 Beam Expander

Considering the small diameter of the laser beam, it was necessary to expand the laser beam in order to fill the objective aperture. Because the objective was diffraction limited, the focus spot size and consequently the excitation volume depend on how much the entrance beam filled the entrance aperture. The beam expander was an inverse Galilean telescope built with a planoconvex lens PLCX – 25.4 – 206.8 – uv – 532 (manufacturer's specified focal length of 206.8 mm) and a planoconcave lens PLCC – 10.0 – 10.3 uv – 532 (manufacturer's specified focal length of 10.3 mm). Both lenses were purchased from CVI laser with anti-reflection coatings at 532 nm. The calculated magnification for this arrangement was 20. Therefore for a 0.2 mm exit beam diameter, the calculated beam diameter after the beam expander was 4 mm. However, due to the initial high beam divergence, the measured beam diameter at the entrance aperture of the objective was 4.5 mm.

A longer focal length planoconvex lens would have been chosen to give a higher beam diameter. However, this would require longer lens tube and as such would increase the overall dimensions of the detector.

2.2.3 Dichroic Mirror

To ease alignment difficulties and reduce cost for collection optics, the epi-illumination mode was chosen for the detector. Therefore a dichroic mirror was incorporated into the optical setup. The mirror was obtained from CVI laser and was such that when inclined at 45^{o} would reflect 532 nm but transmit ultraviolet in the range (280 – 400 nm).

According to the manufacturer, the reflectance at 532 nm was greater than 99.5% while the transmittance at 370 nm was greater than 80%. The mirror substrate was fused silica and had a thickness of 1/4 inches. One disadvantage of using such a thick mirror was that of a big offset of the collected beam from the center after passing through the mirror due to refraction. This is illustrated in the figure and calculations below:

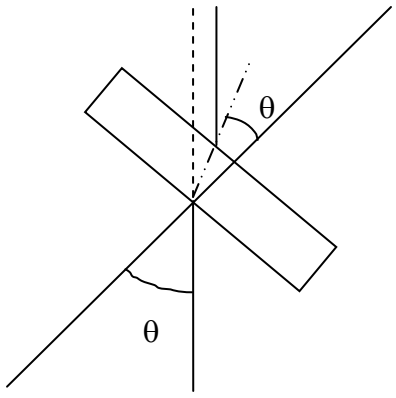

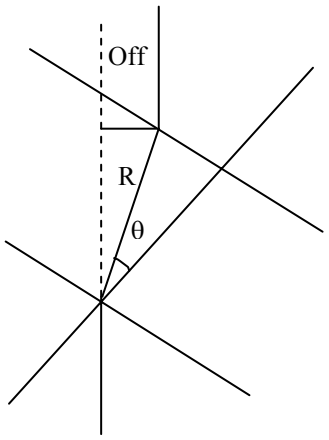

Figure 2–3 Illustration of the emission beam off-set due to refraction after passing through the dichroic mirror.

Wavelength (nm)	Refractive Index (η)
532	1.4607
400	1.47012
355	1.47612
370	?

By using Cauchy's equation [7] below to approximate the refractive index

$$\eta = A + \frac{B}{\lambda^2} + \frac{C}{\lambda^4} + ... \qquad (2-2)$$

Where A, B and C are constants and l is the wavelength, for the data above;

A = 1.443346

B = 5541

C = -178056587

Refractive index of substrate at 370 nm = 1.4743

$$\eta_1 \sin\theta_1 = \eta_2 \sin\theta_2$$
$$\theta_1 = 45^\circ$$
$$\eta_1 = 1$$
$$\eta_2 = 1.4743$$
$$\theta_2 = \sin^{-1}\left(\frac{\eta_1}{\eta_2}\sin\theta_1\right) = 28.67^\circ$$
$$R\cos 28.67^\circ = 6.35$$
$$\therefore R = 7.23mm$$
$$Off = 7.23\sin(45^\circ - 28.67^\circ) = 2.03mm$$

Hence the offset of the collected beam (emission) from the axis of the center beam was 2.03 mm.

The implication of this beam offset was that subsequent optical elements after the mirror had their centers moved by 2.03 mm from the center of the excitation axis for proper alignment. To accomplish this, the detector was fitted with an *x-y* micrometer translation stage (Thorlabs) to correct for this deviation and ensure proper alignment.

2.2.4 Microscope Objective

To achieve a tight focus, an LMU 20X – UV Optics for Research (OFR) microscope objective was used. The objective had a working distance of 4 mm to make sure that the sample and not the sample container is on the focal plane of the objective. The numerical aperture was 0.4, and the effective focal length was 10 mm, while the entrance aperture was 8 mm. Other important specifications of the objective were a design spectrum of 193 – 450 nm, and a theoretical focal spot diameter of 1 μm. To obtain this focal spot diameter, the entrance aperture must be filled. For the case of the detector described here, the focused spot size was expected to be larger than 1 μm as illustrated below. If we assume an airy disc pattern [8], then the waist ω_o could be approximated by the formula:

$$\omega_o = \frac{0.61\lambda}{NA}$$

Where NA is the numerical aperture of the objective and λ is the wavelength. Consider the figure below for the case where the objective's entrance aperture was filled:

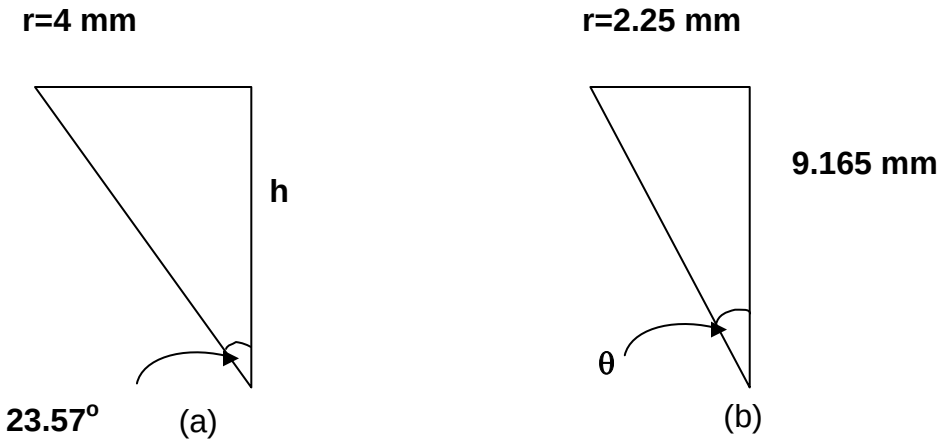

Figure 2–4. Diagrams Illustrating the relationship between entrance beam aperture and numerical aperture of a microscope objective:
(a) With aperture filled completely (8 mm) (b) With partial filled aperture (4.5 mm).

$$NA = \eta \sin\theta$$
$$NA = 0.4$$
$$\eta = 1$$
$$\therefore \theta = \sin^{-1}(0.4) = 23.57^{\circ}$$
$$h = \frac{4}{\tan 23.57^{\circ}} = 9.165mm$$

If we now consider the case with the setup described in this paper; where the diameter of our entrance beam was 4.5 mm, then the effective numerical aperture was calculated as follows:

$$h = 9.165mm$$
$$\theta = \tan\left(\frac{2.25}{9.165}\right) = 13.79^{\circ}$$
$$\therefore NA = \sin 13.79^{\circ} = 0.238$$

Using this effective NA and the laser wavelength of 532 nm in the airy disc equation the waist was calculated to be 1.36 μm which resulted to a beam diameter of **2.72 μm**. Experiments performed to determine the actual waist and volume will be discussed later. However, it should be noted that the above effective numerical aperture was for focusing of the laser. The one specified by the manufacturer, 0.4, was still valid for the emission collection.

2.2.5 Optical Filter

The long *blue-shift* between the excitation and the emission allowed for an easy selection of the optical filter. A filter of choice would attenuate the excitation and other visible wavelengths while passing the uv. A colored glass UG-11 filter was chosen for this setup. Below is the transmission curve of a typical UG-11 colored glass filter [9]. From

the transmission curve, it was obvious that this filter would be a good choice for the detector considering the excitation and emission wavelengths and also room light interferences.

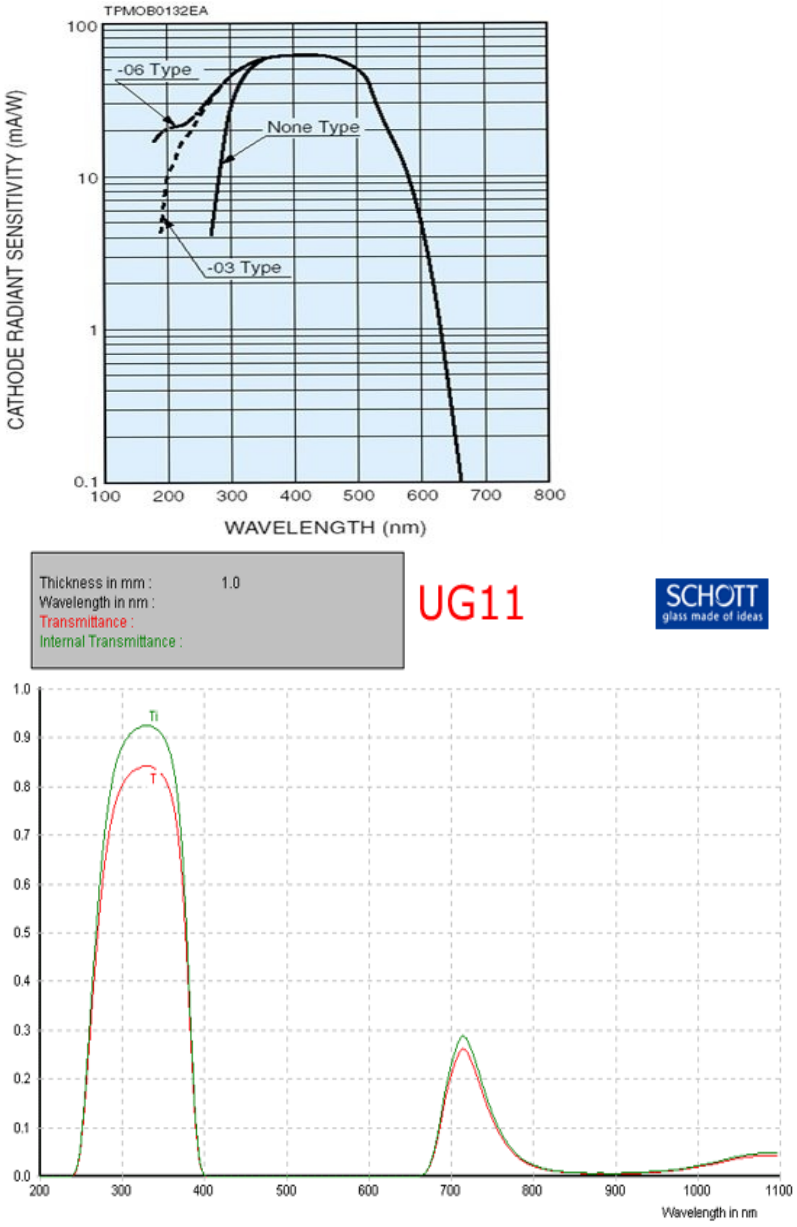

Figure 2–5. Typical cathode radiant sensitivity curve a Hamamatsu H6780 type 03 photomultiplier tube and the transmission curve of a colored glass UG11 optical filter.

2.2.6 Focusing (Tube) Lens

An Optics for research (OFR) LAU-10-100-UVB-Z air-spaced achromatic doublet lens was used to focus the light unto a pinhole. The focal length of the lens was 100 mm. The placement of the lens with respect to the distance from the microscope objective was not critical because the beam emerging from the objective was collimated.

2.2.7 Spatial Filter

A 150 micron pinhole was used as a spatial filter. Though it could be argued that in TPE excitation events only occur at the focal spot of the beam, and as such there will not be need for spatial filtering [10]. However, a large decrease in background signal and a high increase in signal to background ratio were observed when a pinhole was placed on the optical path of the emission beam before impinging on the PMT. Similarly, references abound where spatial filters have been used in TPE setups [8, 11 – 12]. The reason for such a high background level could not be properly ascertained yet, but could be due to auto-fluorescence from the UG11 optical filter or perhaps Raman scattering. Nevertheless, the photomultiplier tube is not quite responsive at wavelengths above 670 nm.

2.2.8 Photomultiplier Tube

A Hamamatsu H6780 type 03 photosensor module was used. This photosensor module is compact and requires a small external dc voltage to operate. The dc power supply was locally built following the manufacturer's recommended circuit diagram. Important specifications of the photosensor module include cathode luminous sensitivity of 67.8

μA/lm; blue sensitivity index of 9.0; anode luminous sensitivity of 36.9 A/lm; dark current of 0.24 nA; and rise time of 0.78 ns. The cathode radiant sensitivity at the peak emission wavelength was 60 mA/W. The module was operated at a gain of 1 million.

2.2.9 Photodiode

In order to properly trigger the data acquisition and signal processing electronics, the weakly transmitted laser light through the dichroic mirror was detected with a biased Thorlabs DET210 photodiode. Figure 2 – 6 shows the photodiode output waveform.

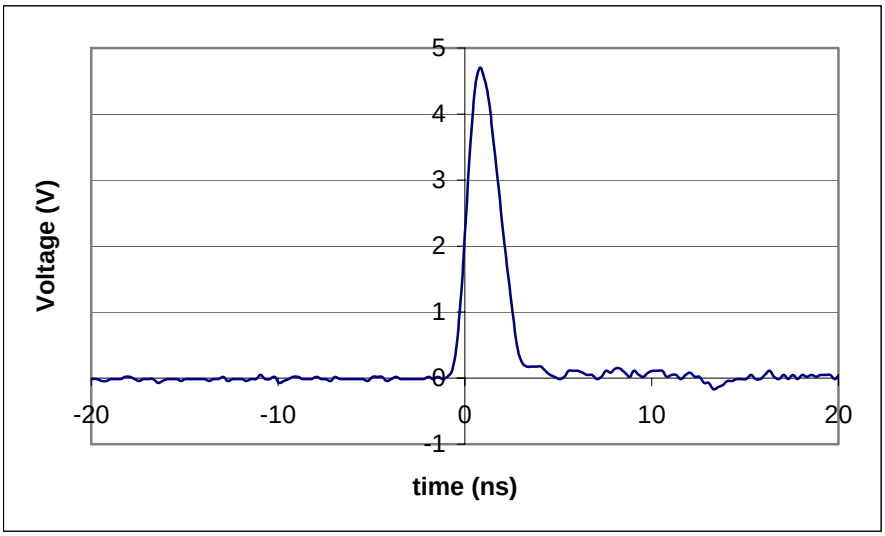

Figure 2-6. Waveform of the biased photodiode signal due to transmitted laser light through the dichroic mirror. The signal was used to trigger the data acquisition instruments.

2.3 Data Acquisition and Signal Processing

The major data acquisition and processing hardware included a LeCroy digital oscilloscope (Waverunner LT372), a Stanford Research gated integrator and boxcar averager (SR250), and a Stanford Research gated photon counter (SR400). The Waverunner and the photon counter were interfaced to a personal computer through GPIB connection while the output of the boxcar was connected to the computer through a National Instrument NI-DAQ BNC 2110. In house programmed National Instruments labview driver programs were used to control and acquire data from the Stanford Research SR 400 gated photon counter. All acquired data were then processed with a Microsoft Excel spreadsheet program.

Data were acquired either in digital mode (photon counting mode) or analog mode (using the boxcar). In the photon counting mode, the signal pulses due to the photon pulses were amplified by a Sonoma Instrument 310 32dB amplifier. The amplified signal was delayed with an HP 180 ns analog delay line. The reason for the delay was that the PMT's rise time was 0.78 ns while the minimum insertion delay of the photon counter was 25 ns. The delayed signal was then connected to the signal input of the photon counter. The output of the photodiode was split into two and was connected to the trigger inputs of the photon counter and the oscilloscope respectively, while the gate and discriminator outputs of the photon counter were connected to inputs 1 and 2 of the oscilloscope respectively. For analog measurements, the connections were similar except that the photon counter was replaced by the boxcar. For this setup, the photodiode signal

was used to trigger the boxcar while the boxcar busy output was used to trigger the oscilloscope. The gate and signal outputs of the boxcar were connected to inputs 1 and 2 of the oscilloscope respectively while the averaged output of the boxcar was connected to the computer through the BNC2110. The settings on these instruments depended on the experiment and will be described in subsequent paragraphs.

2.4 Detector Characterization

2.4.1 Sample Container

An NSG Precision Cells, Inc. Type 39 model S 0.1 mm path length flow cell was used for the liquid samples.

2.4.2 Sample Preparation

DL-tryptophan was purchased from Matheson Coleman & Bell, Norwood, Ohio. Tyrosine and tryptophan were purchased from ICN Biomedicals, Ohio. Phenylalanine and bovine serum albumin was purchased from Sigma Aldrich. De-ionized water was obtained from Milli-Q water purifier installed in the lab. Acetate buffer (pH 5.0) was prepared from sodium acetate and glacial acetic acid. A stock solution of 1×10^{-2} M tryptophan in acetate buffer was prepared and dilutions in the range of 1×10^{-5} M to 1×10^{-3} M were made. Also prepared were 1×10^{-2} M tryptophan solutions in water and a phosphate buffer of pH 7.0 respectively. A stock solution of 1×10^{-3} M bovine serum albumin in phosphate buffer pH 7.0 was prepared, from which dilutions were made in the range 1×10^{-4} M to 2×10^{-6} M. The flow cell was rinsed three times with phosphate buffer pH 2.7 followed by rinsing with *de-ionized* water three times. Also prepared were 2 mM stock solutions of tyrosine and phenylalanine in phosphate buffer at pH 7.0. From

the tyrosine stock solution, dilutions were made in the range of 1 x 10^{-3} to 2 x 10^{-4} M. Another 0.05 M stock solution of phenylaline was prepared in pH 7.0 phosphate buffer. From this solution, dilutions were made in the range of 0.005 to 0.05 M.

2.4.3 First Test

After assembling and aligning the detector optics, the first thing was to determine if the detector was capable of causing TPE excited fluorescence of the aromatic amino acids and also detect the corresponding emission. This was done by connecting the amplifier and photodiode outputs to the oscilloscope's channel 1 and external trigger inputs respectively. Then, tryptophan powder on a watch glass was place on the focal plane of the microscope objective. This resulted in a very high signal level that saturated the PMT. Next, the tryptophan powder was replaced with sodium acetate powder, in this case, no signal was observed. This simple experiment confirmed that the detector was capable of causing TPE excited fluorescence of aromatic amino acids and proteins with good discrimination of background fluorescence and scattered radiation from the matrix.

Following the success with the powder, a 0.002 M solution of tryptophan in phosphate buffer pH 7.0 was then placed on a flow cell. The waveform obtained for the solution and that of phosphate solution as blank are shown on figure 2 – 7. The results here also showed that the detector responded to signal from the tryptophan as opposed to that from the buffer. This was a further proof that the detector would detect proteins and aromatic amino acids.

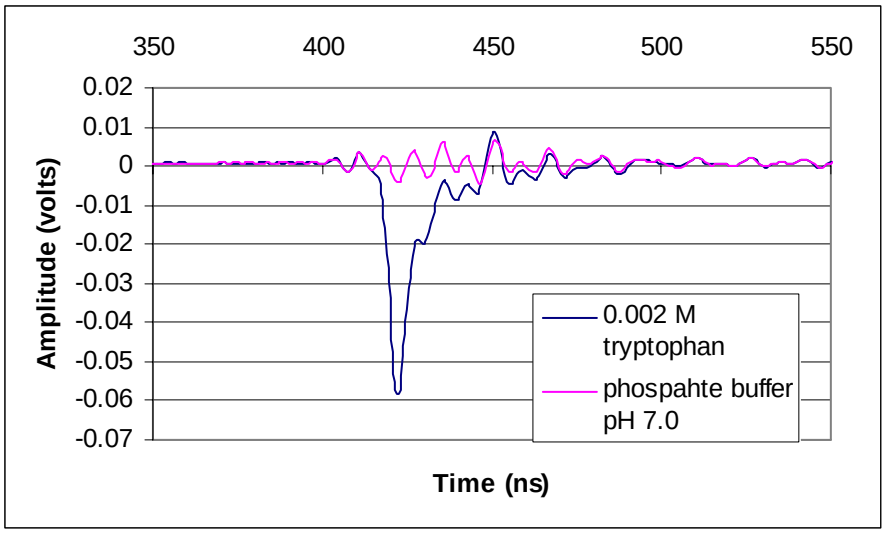

Figure 2–7. Waveform of 2 mM tryptophan and pH 7.0 phosphate buffer used as a blank. It is clear from these waveforms that the observed signal was from the tryptophan and not from the solvent.

The detector was not equipped with an eye piece, but had just an *x*-*y*-*z* translation stage. To make sure that the sample was correctly positioned at the focal plane of the microscope objective, the boxcar averaged output (1000 samples) was recorded while the separation between the microscope objective and the flow cell was scanned by manually translating the z-micrometer with the flow cell empty, filled with pH 7.0 buffer and filled with 0.01 M tryptophan respectively. Figure 2 – 8 shows the plots of the micrometer reading against the boxcar output. The flow cell consisted of two quartz plates sandwiched together with a 0.1 mm groove inside to hold a fluid. The first peak represents reflection from the bottom surface of the flow cell, while the second peak represents reflection from the bottom-inner surface of the flow cell. The third peak represents the top-inner surface of the flow cell while the fourth peak represents the top surface of the cell. The window between the two inner peaks represents the path length of the flow cell. As can be seen in the figure, in this window, the signal from the tryptophan was optimum. Hence by leaving the dial on the *z*-micrometer within this window ensured that the sample but not the flow cell was on the focal plane of the microscope objective.

After determining the correct vertical position to ensure that the sample was on the focal plane of the objective, this position became the location for the flow cell for all subsequent experiments.

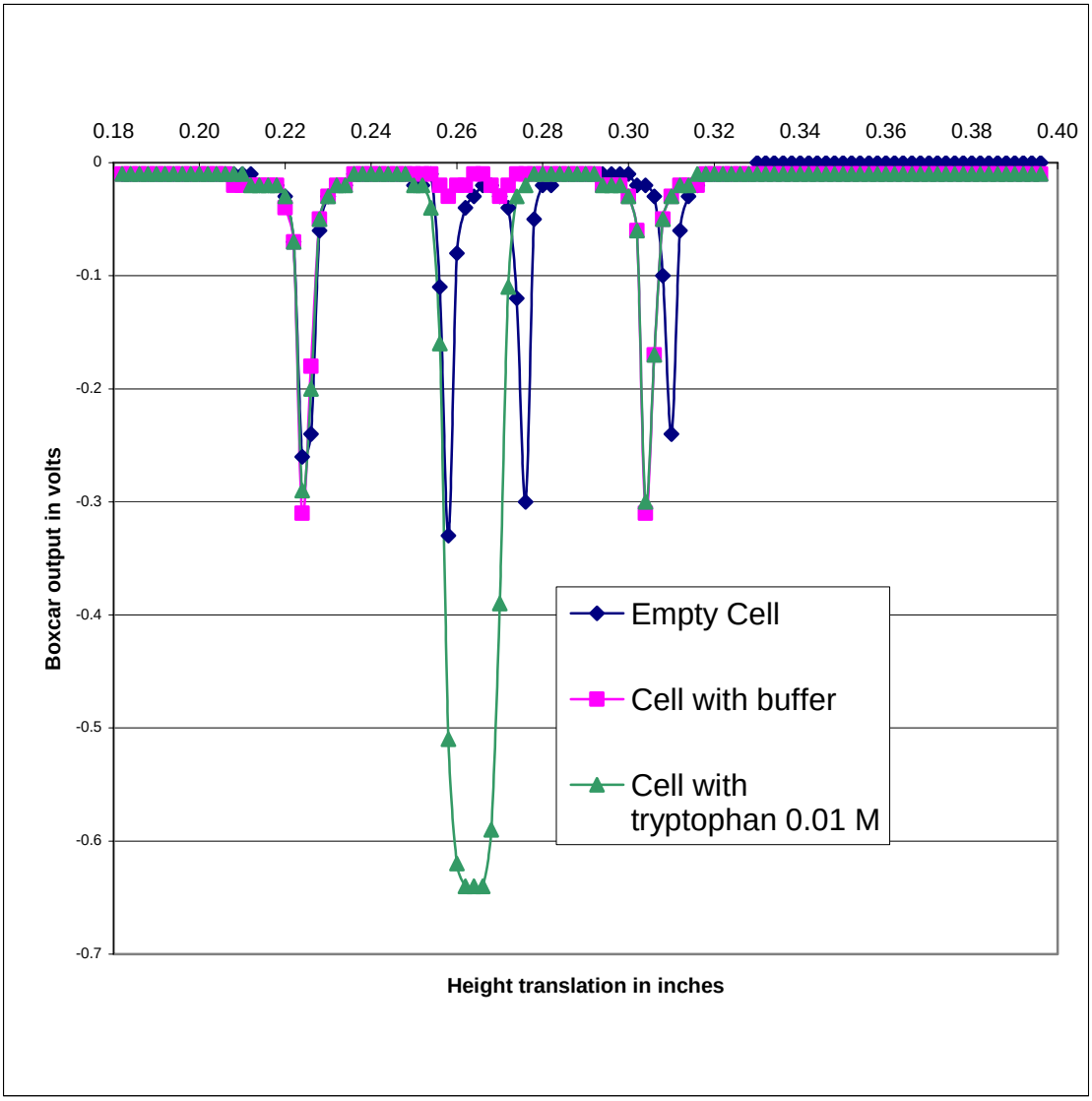

Figure 2 – 8. Signal variation with respect to the distance between the microscope objective and the flow cell. The abscissa represents the dial on the *z*-micrometer as the objective was scanned away from the top of the flow cell.

Other experiments performed to characterize the detector include: determination of source of background and signal to noise analysis; determination of detection limits of the detector relative to the three fluorescent amino acids – tryptophan, tyrosine, and phenylalanine, and some selected proteins; and the determination of the excitation volume by a photon counting histogram technique. In these experiments, the sample was placed on a type 49 code S 0.1 mm quartz flow cell from NSG Precision Cells, Inc. (see figures 2 – 1 and 2 – 2). Photon counting was used because of the low light levels observed. The settings on the photon counter varied and were relative to the experiments performed. Settings specific to a certain experiment will be given in the proper section or paragraph. These experiments will now be discussed with the exception of excitation volume determination, which will be given in chapter 3.

2.4.4 Source of Background and Signal to Noise Analysis

The determination of background sources and signal-to-noise analysis were significant in characterizing the detector, as these factors are among the figures of merit of a good detector. Gated photon counting was employed in the experiments described in this section. The gate delay and width were set by connecting the 'A' gate and 'A' discriminator outputs of the photon counter to input channels '1' and '2' of the LeCroy oscilloscope using cables of equal length. The gate delay and width were adjusted until the gate waveform (displayed on the scope) corresponded to the discriminator time with a slightly wider width. This resulted in a gate delay of 94 ns and a width less than 34 ns.

2.4.5 Pulse Height Distribution

Before the commencement of the noise experiment, the first thing that was done was to obtain a pulse-height-distribution to determine the optimum photon counter discriminator level that would discriminate against the PMT dark current, anode ringing and jitter but not against signal pulses. Though a multi-channel analyzer was not available, the procedure suggested in the SR400 user's manual was used.

Briefly, the procedure consisted of turning on the laser and all other associated instruments including the photon counter. The sample holder was filled with a tryptophan solution to allow sufficient light to impinge on the photo multiplier tube. The gate delay and width were properly set to 94 ns and 34 ns respectively to discriminate against pulses that are not within this time window. Then the photon counter input was set to counter A and B while the T counter was preset to count the trigger – 10000 triggers, this was more than the laser repetition rate (6.56 kHz) but was enough to provide good statistical data. Then the A and B discriminators were scanned and a plot of A-B was then obtained. The point where the minimum occurred was the optimum discriminator level which when used would reduce the counting of dark counts, anode ringing and jitter without discriminating against the signal photons. This was found to be approximately -20 mV (see figure 2–9).

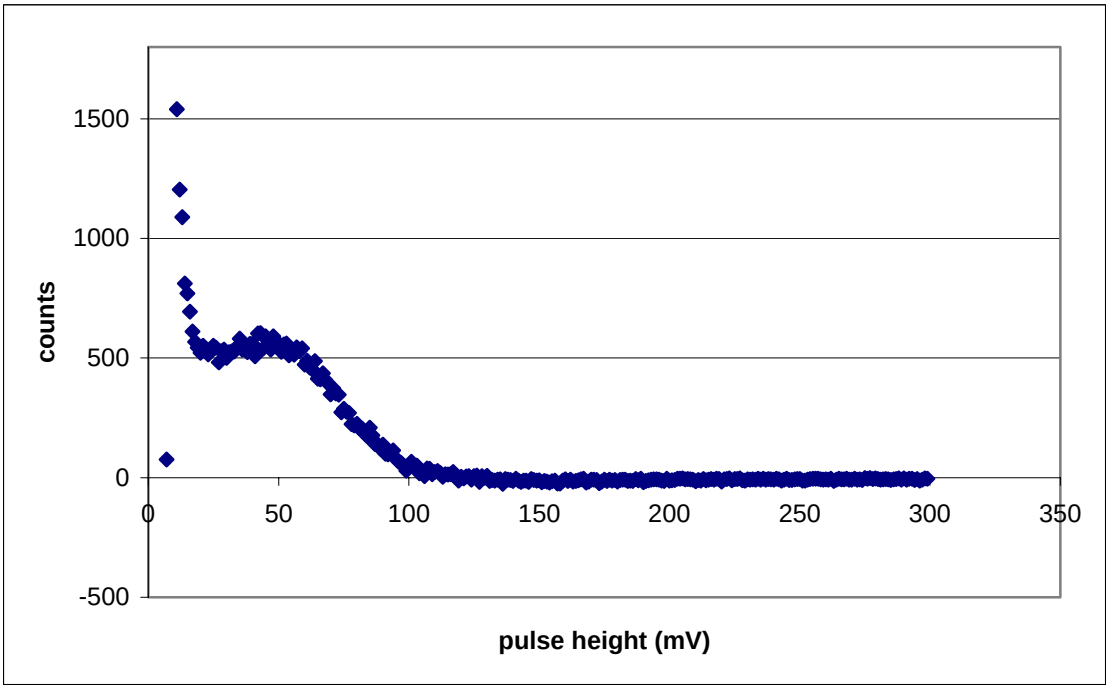

Figure 2–9. Pulse height distribution to determine the optimum discriminator level that will discriminate against photomultiplier tube dark counts, anode ringing and jitter in the cables without discriminating against the signal. The optimum was found to be -20 mV.

2.4.6 Background Signals

The first measurement of the background signal was done by turning on the detector and then blocking the PMT. With the photon counter set at the levels obtained above except that the T counter was preset to count 7000 triggers, a zero count was recorded for more than 200 count periods. This showed that the settings on the photon counter were discriminating the dark current and anode ringing of the PMT.

2.4.7 Background Signal Analysis

Next, the block on the PMT was removed, but the size of the spatial filter was changed from 150 μm to 1 mm and then to 1.5 mm. With each spatial filter, photon counts were obtained with the flow cell removed (representing instrument dark count), with the flow cell filled with phosphate buffer (representing blank count), and with the flow cell filled with 0.05 M phenylalanine (representing signal counts). The result of this experiment is shown in table 2-1. As the table shows, reducing the size of the spatial filter from 1.5 mm to 1 mm, reduced the instrument dark count by 54% while the background and signal counts decreased by 46% and 19% respectively. Similarly, reducing the size of the spatial filter from 1 mm to 150 μm decreased the dark and background counts reduced by 97% while the signal decreased by 52%. One obvious conclusion that could be drawn from the above result is that the optical filter was not effective in completely filtering the background signals. Perhaps the background could be due to auto-fluorescence from the optical filter. However, the result of an experiment done with two UG11 filters spatially separated did not show a significant reduction in the background signal, thereby making it hard to conclude that auto-fluorescence from the UG11 filter could be the major source of the background

	Average counts/s			
	150 μm pinhole	1 mm Iris	1.5 mm Iris	
No flow cell	1	29	64	
blank	52	1691	3156	
0.05 M phenyalanine	2126	6006	8453	
analyte signal (less blank)	2073	4315	5297	
Background reduction from 1mm iris to 150 micron pinhole	97%		Dark reduction from 1mm iris to 150 micron pinhole	97%
signal reduction from 1mm iris to 150 micron pinhole	52%			
Background reduction from 1.5 mm iris to 150 micron pinhole	98%		Dark reduction from 1.5 mm iris to 150 micron pinhole	99%
signal reduction from 1.5 mm iris to 150 micron pinhole	61%			
Background reduction from 1.5 mm iris to 1 mm Iris	46%		Dark reduction from 1.5 mm iris to 1 mm Iris	54%
signal reduction from 1.5 mm iris to 1 mm Iris	19%			

Table 2 – 1. Experimental results of the change in the magnitude of the dark, analyte and background signals as the size of the spatial filter was varied

signal. It is also possible that the background could be due to Raman scattering, since the major Raman peak for water at the wavelength of the laser occurs at 649 nm. However the PMT has poor sensitivity at this wavelength, and this wavelength is close to the cut-off of the UG11 filter. Therefore to reduce the background signal by tightening the spatial filtering came with a price – losing some of the analytical signal. A possible solution to this problem would be to add a short pass optical filter in addition to the UG11 filter to help reduce and attenuate the background but not the analyte signal.

Another experiment done was aimed at seeing how the signal and the background varied by changing the thickness of the UG11 filter from 2 mm to 3 mm (50% increase in filter thickness). The results obtained showed a 10% decrease in both the signal and background counts.

At this point, it would have been interesting to obtain a spectrum of the background for a guide in choosing the short pass filter. However, this was not done because of instrument constraints. Nevertheless, from the emission spectra of the three amino acids shown in chapter one, a cut-off of 400 nm would be good.

Because the UG11 filter was the only filter available, the 2 mm thick filter and the 150 μm pinhole were chosen for subsequent experiments including detection limits determination. This choice was based on the fact that the 150 μm offered higher signal-to-noise ratio and also higher signal-to-background ratio than the other two spatial filters.

One could perhaps think that it would be better in this case to choose a larger size spatial filter since it does not attenuate the analytical signal.

However, with compounds with higher quantum yields, it was very easy to get photon pile-up that was not due to analyte signal but due to the high background photons. This would then make photon counting difficult. Also the recovery of weak analytical signals would be difficult since they would be buried in large background. A better option would be to get a good filter combination that would attenuate the background and then do away with the spatial filter, since two-photon events only occur at the focal point of the objective where the intensity is optimum.

2.4.8 Signal-to-Noise Characterization

The table 2-2 shows the data used to perform the signal-to-noise analysis in the photon counting mode for tryptophan and tyrosine while Figure 2-10 shows the plot of signal-to-noise against average signal with increasing concentration for the two analytes respectively. Both the data and the graph show that for tryptophan, the signal-to-noise was not limited by shot noise as the noise was higher than the square-root of the signal. A closer look at the graph shows that there are perhaps two regions. The first region is where the signal-to-noise is proportional to the analyte signal. This meant that the blank noise was dominant at these concentrations. The second region is where the signal-to-noise is independent of the analyte signal.

There is a direct proportionality between signal-to-noise ratio and the analytical signal in the case of tyrosine. However, the slope of the line is 0.5 within the limits of

experimental error. Because the slope is equal to 0.5, the noise is limited by shot noise since signal-to-noise ratio is proportional to the square-root of the signal in shot noise limited cases:

$$(S/N) \propto \sqrt{n}$$
$$(S/N) = k\sqrt{n}$$
$$(S/N)^2 = k^2 n$$
$$\therefore \log(S/N) = \log k + 0.5 \log n$$

Tryptophan Concentration (M)	Average Signal (S)	Standard Deviation (N)	Square Root of S	Signal to Noise Ratio (S/N)	Signal to Background Ratio (S/B)
1.00E-05	86.20	29.45	9.28	2.93	2.24
5.00E-05	284.60	63.66	16.87	4.47	7.41
8.00E-05	370.60	31.59	19.25	11.73	9.65
1.00E-04	474.50	25.44	21.78	18.65	12.36
2.00E-04	772.50	40.82	27.79	18.92	20.11
3.00E-04	1267.40	85.06	35.60	14.90	33.00
Blank (B)	38.41	6.05	6.20	6.34	

(A)

Tyrosine Concentration (M)	Average Signal (S)	Standard Deviation (N)	Square Root of S	Signal to Noise Ratio (S/N)	Signal to Background Ratio (S/B)
4.00E-04	123.45	12.11	11.11	10.19	3.21
6.00E-04	202.40	12.39	14.23	16.34	5.27
1.00E-03	459.95	23.05	21.45	19.95	11.98
2.00E-03	1366.80	30.82	36.97	44.35	35.59
Blank (B)	38.41	6.05	6.20	6.34	

(B)

Table 2-2. Data for the analysis of signal-to-noise and signal-to-background for (A) tryptophan (B) tyrosine

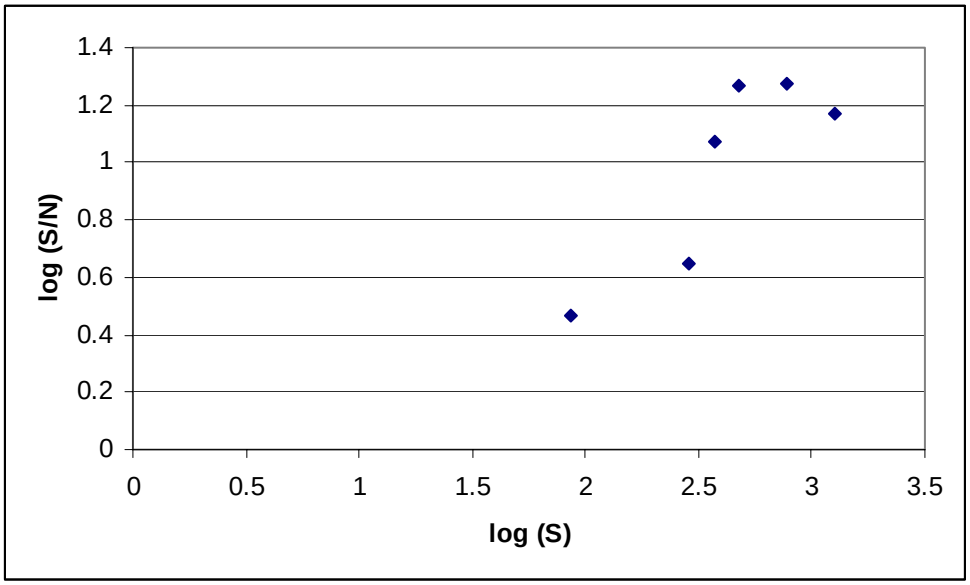

(A)

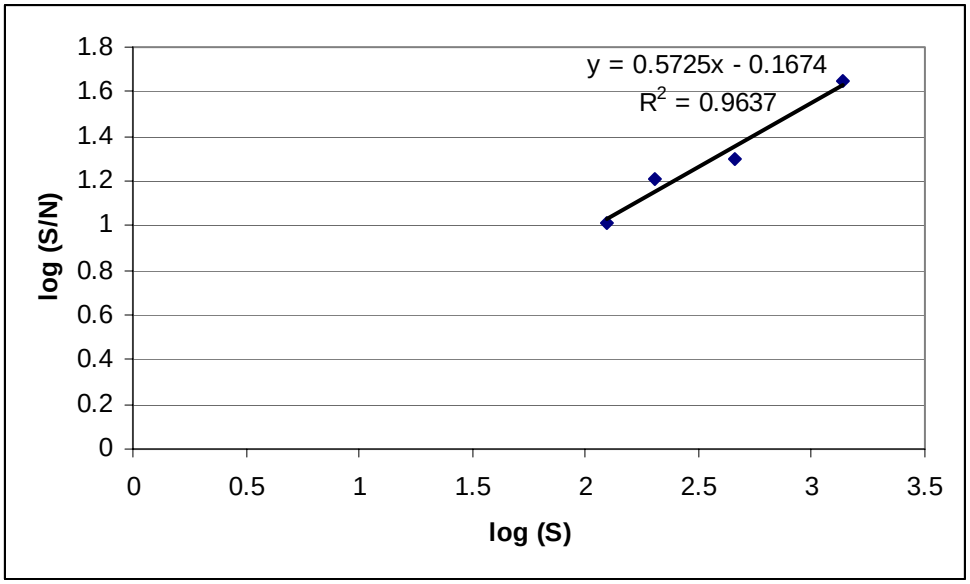

(B)

Figure 2–10. Plots of log of signal-to-noise ratio (S/N) against log of signal (S) (photon counts) with increasing concentration for (A) tryptophan and (B) tyrosine.

2.4.9 Determination of Detection Limit(s) and Linear Dynamic Range(s) for the Aromatic Amino Acids.

The amino acids were respectively dissolved in phosphate buffer pH 7.0. The solutions were carefully prepared and de-aerated before making the fluorescence measurements. Figure 2-11 shows comparative signals counts of 2 mM tryptophan, tyrosine, phenylalanine and phosphate buffer pH 7.0. The observed distribution of the signals reflects the differences in the two-photon absorption cross-sections of these amino acids. Please note that this distribution was obtained at a different alignment of the detector optics from the one actually used to determine the detection limits. The optics were better aligned during the actual detection limit experiments, thereby giving higher counts for the amino acids but a lower count for the blank.

Figures 2-12, to 2-14 show the calibration curves for tryptophan, tyrosine and phenylalanine respectively. Each data point was obtained by presetting the photon counter T-counter to 7000 laser shots. An average of 10 data points were taken for each concentration while 200 data points were taken for the blank sample. From the slopes of the calibration curves and at three times the standard deviation of the blank, the detection limits for tryptophan, tyrosine and phenylalanine were calculated to be 4.54×10^{-6} M, 2.25×10^{-5} M, and 5.03×10^{-4} M respectively.

The linear dynamic range of tyrosine could be approximated to be from the detection limit (2.25×10^{-5}M) to 2.0×10^{-3} M spanning about two orders of magnitude.

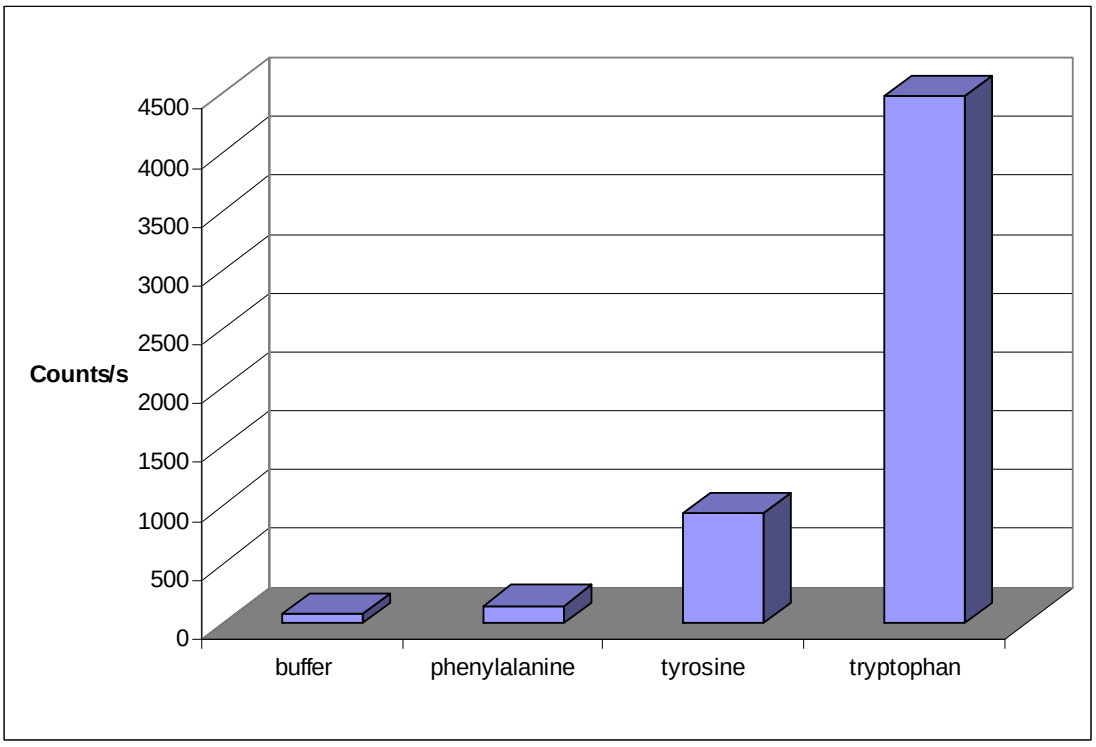

Figure 2-11. Comparative signals of 2 mM tryptophan, tyrosine, phenylalanine and phosphate buffer pH 7.0. The observed distribution of the signals reflects the differences in two-photon absorption cross-sections of these amino acids. The solutions were prepared in phosphate buffer.

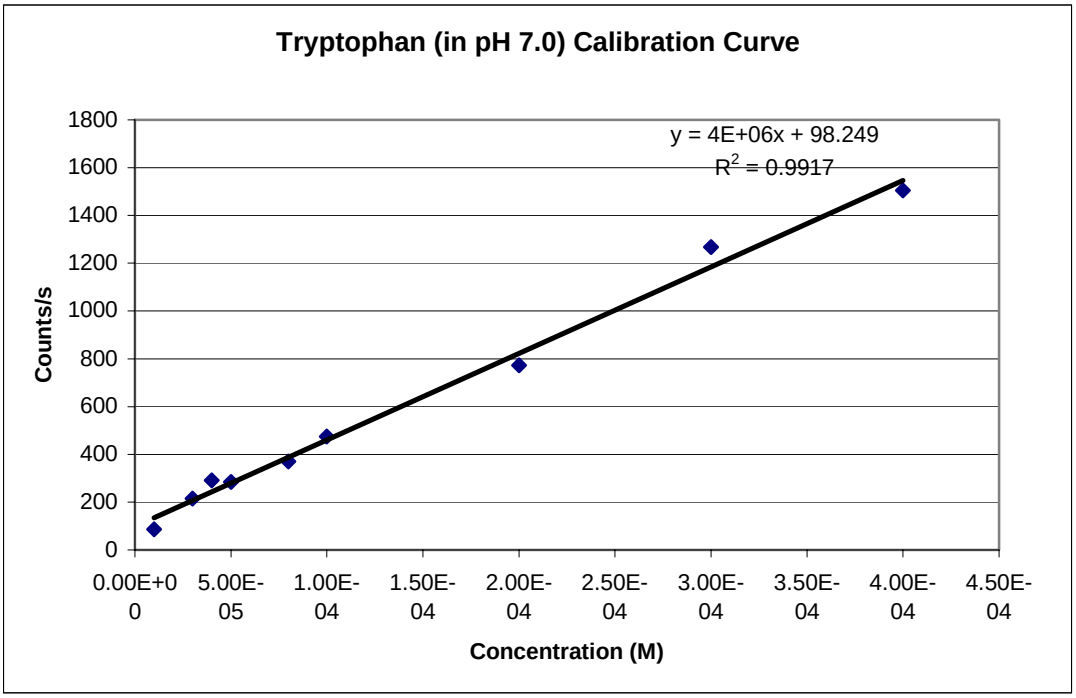

Figure 2 – 12. Tryptophan calibration curve. From this calibration curve, a detection limit of 4.5 μM was calculated at 3-times the standard deviation of the blank.

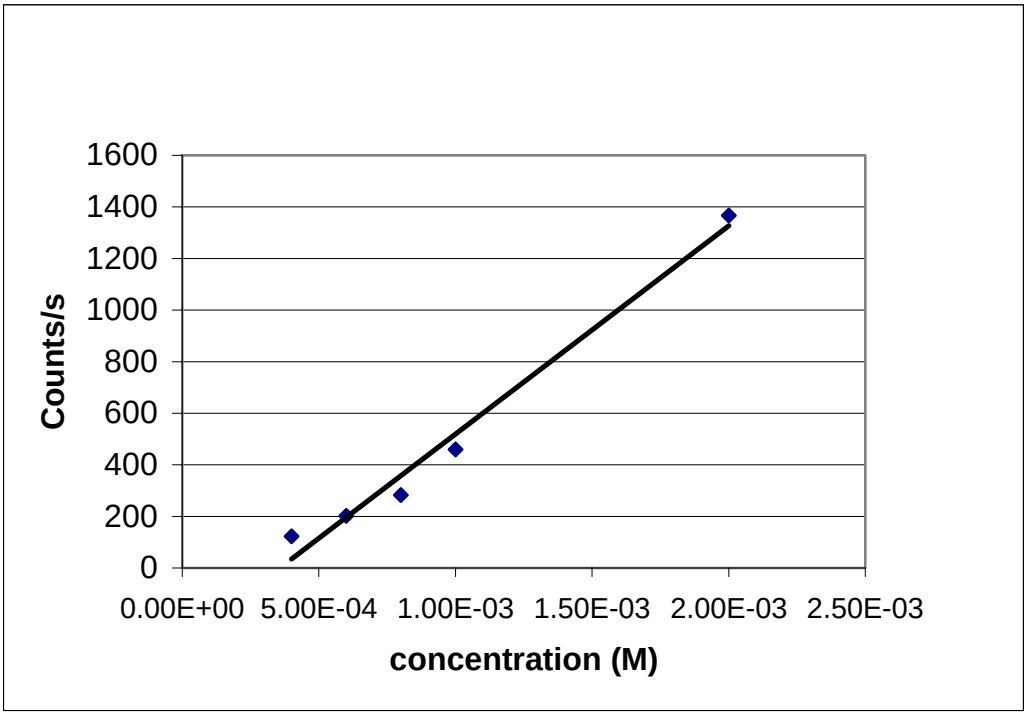

Figure 2-13. Tyrosine calibration curve. From this calibration curve, a detection limit of 22.5 μM was calculated also at 3-times the standard deviation of the blank.

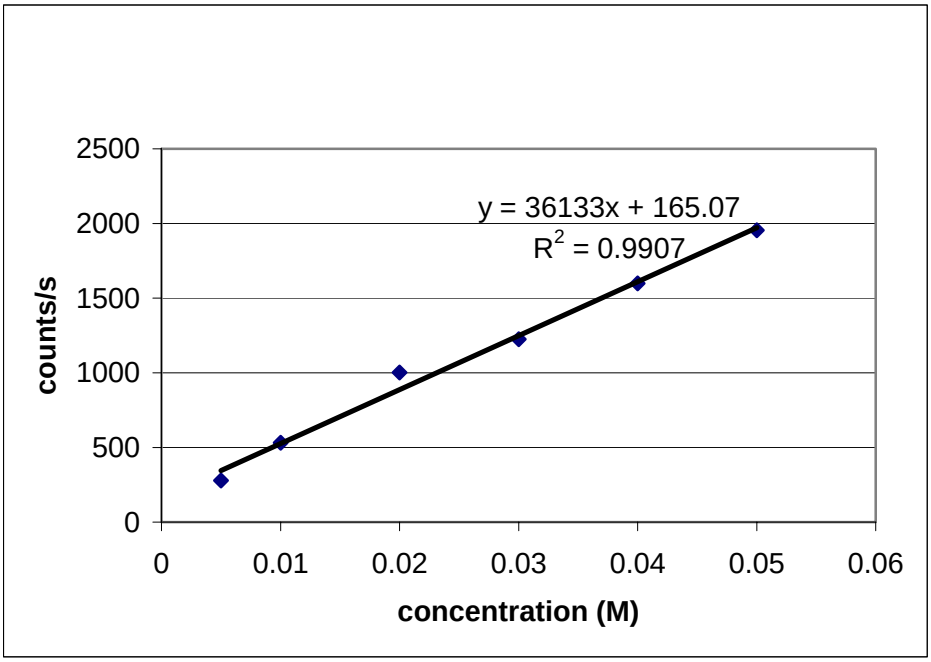

Figure 2-14. Phenylalanine calibration curve. The detection limit was found to be 500 μM at three-times the standard deviation of the blank.

For tryptophan, the linear dynamic range is also from the detection limit, 4.54 x 10^{-6} M to 4.00 x 10^{-4} M, also spanning two orders of magnitude. Similarly, the linear dynamic range for phenylalanine could be approximated to be from the detection limit 5.03 x 10^{-4} M to 0.05 M, also spanning two orders of magnitude. As stated in the previous paragraph, an improvement on the detection limit will improve the linear dynamic range

Though with most fluorescence experiments, the linear dynamic range is usually not very large because of self absorption and quenching at higher concentrations [13]. However, self absorption and quenching would not be limiting the linear dynamic range in this situation, rather photon pile-up will. Photon pile-up arises when two or more photon pulses overlap and are counted as one pulse. This usually happens at higher light levels. Using Poisson probability distribution on a MATCAD worksheet, the following plots show the deviation from linearity at higher count rates when using a photon counter where 6500 is the laser repetition rate:

$$k := 1 .. 10000 \qquad \lambda_k := \frac{k}{6500}$$

$$Counts\_Observed_k := 6500\left(dpois\left(1,\lambda_k\right) + dpois\left(2,\lambda_k\right) + dpois\left(3,\lambda_k\right) + dpois\left(4,\lambda_k\right) + dpois\left(5,\lambda_k\right) + dpois\left(6,\lambda_k\right)\right)$$

$$Counts\_Actual_k := 6500\left(dpois\left(1,\lambda_k\right) + 2\cdot dpois\left(2,\lambda_k\right) + 3\cdot dpois\left(3,\lambda_k\right) + 4\cdot dpois\left(4,\lambda_k\right) + 5\cdot dpois\left(5,\lambda_k\right) + 6\cdot dpois\left(6,\lambda_k\right)\right)$$

$$percent\_error_k := \frac{\left(Counts\_Actual_k - Counts\_Observed_k\right)\cdot 100}{Counts\_Actual_k}$$

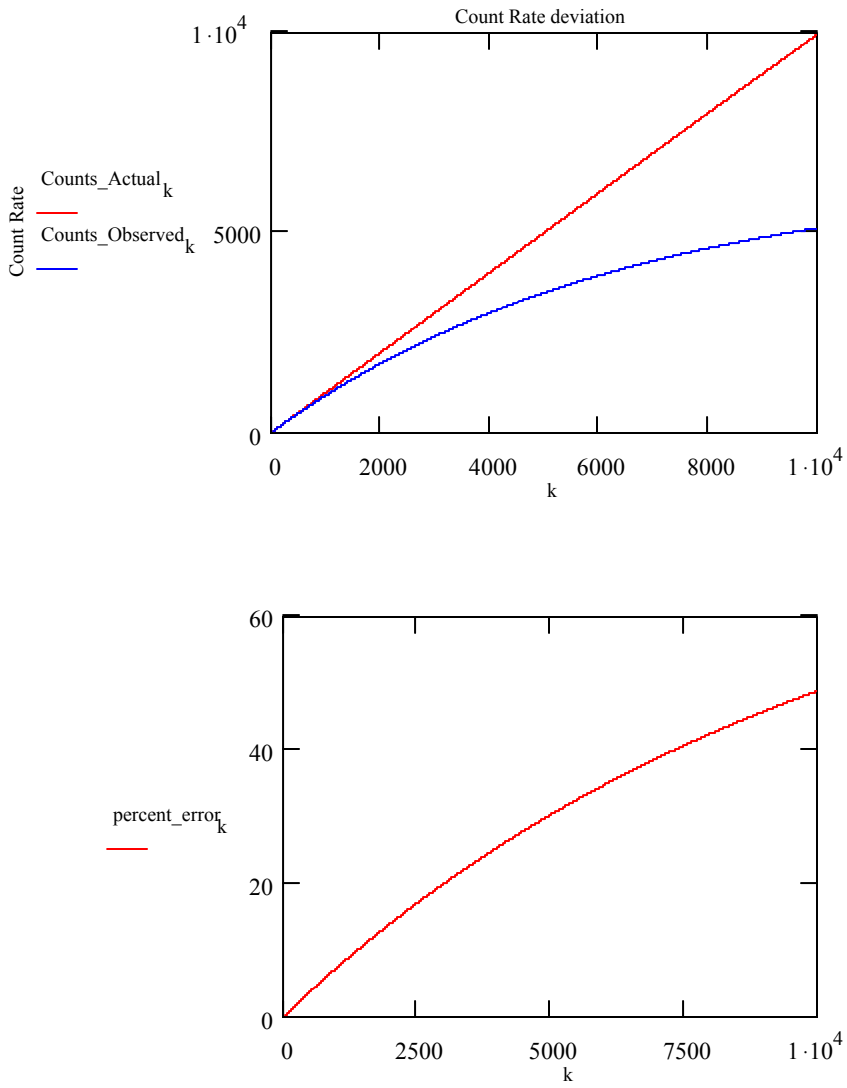

Figure 2-15. Deviation from linearity and percent error due to photon or pulse pile-up with increasing count rates due to increase in light intensity.

Therefore, to improve on the linear dynamic range, a combination of analog detection and photon counting would be required. Use of more than one counter where the

discriminator levels are set differently and then recording the sum of the two counters would also reduce the effect of photon pile-up.

2.4.10 Detection Limit for the Protein Bovine Serum Albumin (BSA)

BSA was a model protein chosen to characterize the detector simply because of its availability. It is a 69,293 Da protein and has the amino acid sequence below [14]:

```
        10         20         30         40         50         60
         |          |          |          |          |          |
MKWVTFISLL LLFSSAYSRG VFRRDTHKSE IAHRFKDLGE EHFKGLVLIA FSQYLQQCPF

        70         80         90        100        110        120
         |          |          |          |          |          |
DEHVKLVNEL TEFAKTCVAD ESHAGCEKSL HTLFGDELCK VASLRETYGD MADCCEKQEP

       130        140        150        160        170        180
         |          |          |          |          |          |
ERNECFLSHK DDSPDLPKLK PDPNTLCDEF KADEKKFWGK YLYEIARRHP YFYAPELLYY

       190        200        210        220        230        240
         |          |          |          |          |          |
ANKYNGVFQE CCQAEDKGAC LLPKIETMRE KVLASSARQR LRCASIQKFG ERALKAWSVA

       250        260        270        280        290        300
         |          |          |          |          |          |
RLSQKFPKAE FVEVTKLVTD LTKVHKECCH GDLLECADDR ADLAKYICDN QDTISSKLKE

       310        320        330        340        350        360
         |          |          |          |          |          |
CCDKPLLEKS HCIAEVEKDA IPENLPPLTA DFAEDKDVCK NYQEAKDAFL GSFLYEYSRR

       370        380        390        400        410        420
         |          |          |          |          |          |
HPEYAVSVLL RLAKEYEATL EECCAKDDPH ACYSTVFDKL KHLVDEPQNL IKQNCDQFEK

       430        440        450        460        470        480
         |          |          |          |          |          |
LGEYGFQNAL IVRYTRKVPQ VSTPTLVEVS RSLGKVGTRC CTKPESERMP CTEDYLSLIL

       490        500        510        520        530        540
         |          |          |          |          |          |
NRLCVLHEKT PVSEKVTKCC TESLVNRRPC FSALTPDETY VPKAFDEKLF TFHADICTLP

       550        560        570        580        590        600
         |          |          |          |          |          |
DTEKQIKKQT ALVELLKHKP KATEEQLKTV MENFVAFVDK CCAADDKEAC FAVEGPKLVV
```

STQTALA

From this sequence, BSA has 3-tryptophan residues, 21-tyrosine residues and 30 phenylalanine residues.

Figure 2-16 shows the calibration curve for BSA. From this calibration curve, the detection limit at 3-times the standard deviation of the blank was found to be 9.08 x 10^{-7} M. The linear dynamic range was approximated to be 2-orders of magnitude from the detection limit.

2.4.11 Photostability/Photobleaching Tests

A photostability/photobleaching test was done on tryptophan just to give an idea on how soon tryptophan starts to photo-degrade or bleach due to the high intense excitation. With tryptophan powder, the signal went to almost zero in less than 3 minutes. Figure 2-17 shows a photostability plot for 10 mM tryptophan solution.

From the figure it could be seen that no significant degradation in tryptophan signal occurred within 33 minutes of constant illumination. The reason for the quick photobleaching of the powder as against that of the solution could be attributed to the fact that equilibrium was maintained due to molecular diffusion occurring in the liquid phase. Also, it is possible for excited molecules to dump their excess energy on the solvent but in the solid phase, the excited molecules do not have anywhere to dump their excess energies.

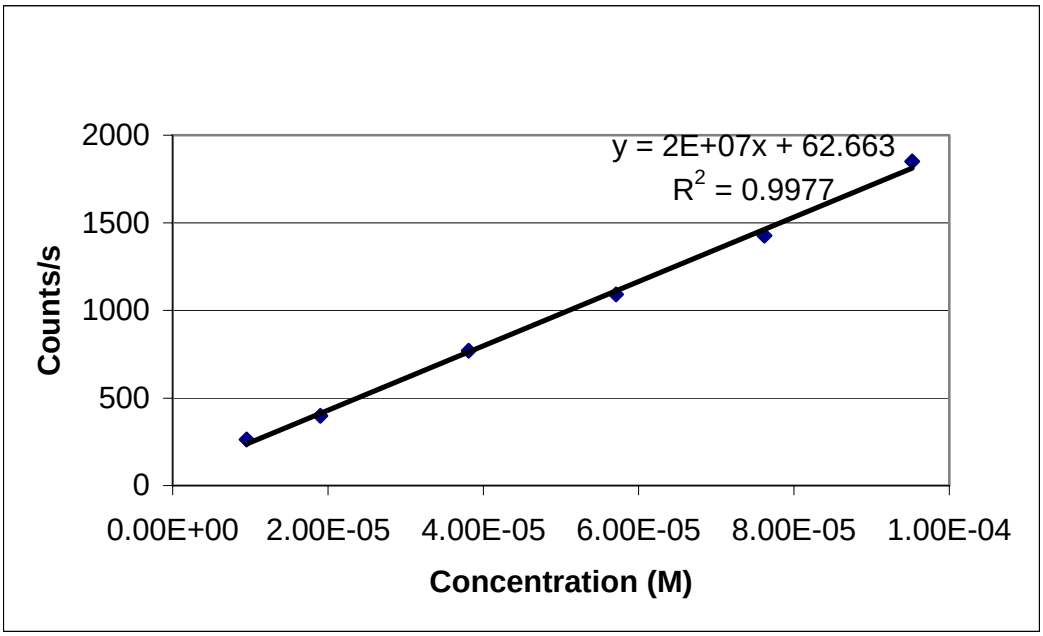

Figure 2-16. Calibration curve for bovine serum albumin. This serum protein has 3 tryptophan residues 21 tyrosine residues and 30 phenylalanine residues. Nevertheless, the calculated detection limit of 9.0 x 10^{-7} M when compared to those of tryptophan and tyrosine indicates that there was significant quenching in the emission of the tryptophan and that of tyrosine. Some of the quenching could be due to energy transfer from tyrosine to tryptophan or to the conformation of the protein at the experimental conditions.

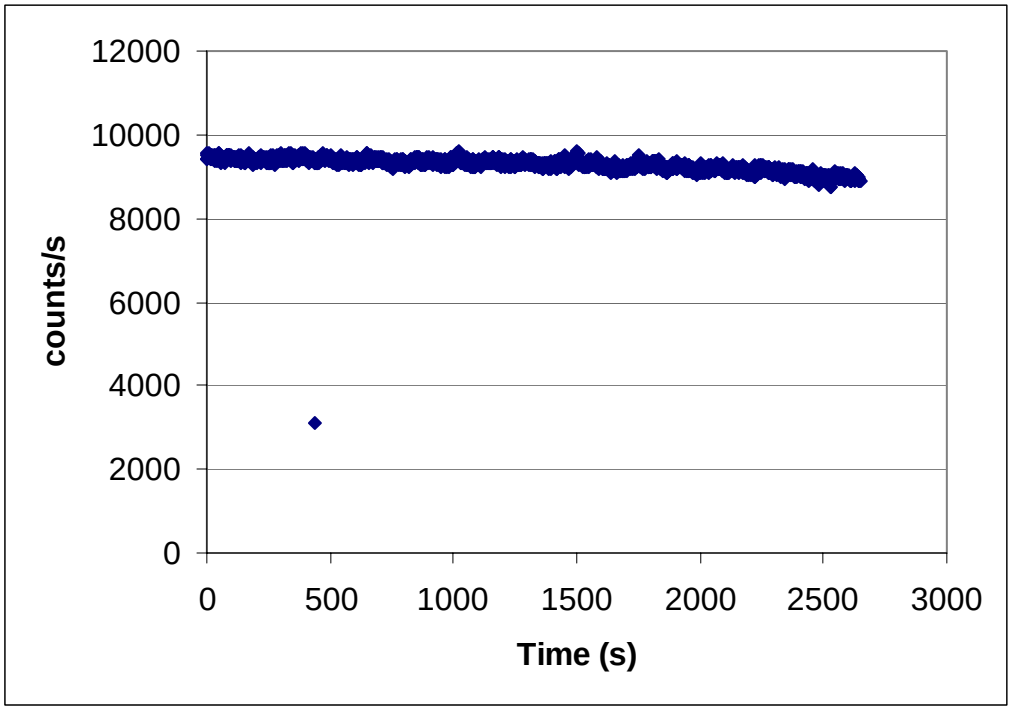

Figure 2-17. Photostability plot of 10 mM tryptophan solution with as a function of time due to TPE. The solution was relatively stable for at least 33 minutes before the emitted photons started to decrease. The low count at 500 s was due to an error from the photon counter as a result of trigger over-range due to auto-re-calibration by the oscilloscope that shared the same trigger source with the photon counter at the time of measurement.

2.5 Discussion

We did not record emission intensity as a function of excitation intensity to show the quadratic dependence of emission intensity upon excitation intensity. However, it could easily be shown that in this particular case that the excitation was due to the absorption of two photons. In any luminescence experiment, in the absence of external light or radiation, there are four sources that could contribute to the observed analytical signal – elastic scattering, inelastic scattering, stray and specular reflection of the light source, and fluorescence. Elastic scattering such as Rayleigh scattering occurs at the same wavelength of the excitation source (in this case it will occur at 532 nm). With the optical filtering provided by the dichroic mirror and the UG11 filter, such scattering signal would be highly attenuated. Moreover, if it was responsible for the observed signal, the sample signal and that of the blank would have been equal.

On the other hand, Raman scattering is red-shifted and the Raman band (λ_R) is given by:

$$\lambda_R = \frac{\lambda}{1 + \lambda \Delta \bar{\upsilon}} \qquad (2 - 3)$$

Where λ is as defined previously and $\Delta \bar{\upsilon}$ is the Raman shift in nm^{-1}. If we take the Raman shift for water to be 0.339 μm^{-1}, then according to equation (2 - 3), the Raman band in this case will occur at 649 nm. The PMT used is slightly responsive at this wavelength and it is also close to transmission window of the UG11 optical filter. It is possible that some Raman signal may be detected and could be the reason for the high background count. However, the analytical signal was not that of Raman since the blank signal was well below that observed with the analyte. Also, because the aromatic amino

acids absorb in the UV, it is clear that such an emission signal recorded by the instrument must not be due to single photon absorption. Rather, it was due to multi-photon absorption, and in this case in can be concluded that it was due to two photon absorption of 532 nm wavelength each corresponding to the electronic transition of 266 nm.

Another confirmation that the observed signals were due to multiphoton excitation comes from the large analog signal recorded when tryptophan powder was placed on the focal plane of the detector against virtually no signal recorded with sodium acetate powder.

The detection limits reported here for tryptophan and tyrosine were about an order of magnitude higher (in molar terms) than the one reported by *Shear et al* [15], where he used a more elaborate and expensive laser system. Nevertheless, the detection limit could still be improved by addressing the issues raised earlier on the challenges with the present optical setup. Such challenges included the use of a tight spatial filter (a consequence of the high background counts). As shown in the previous paragraph, more than 50% of the analyte signal was lost with this size of spatial filter. By eliminating the use of a spatial filter, and by choosing a good optical filter combination, the detection limits could be further reduced by at least 50%.

Other challenges include high beam divergence even after the laser beam diameter was expanded to 4 mm. This made the beam diameter entering the objective's entrance aperture to be 4.5 mm just after the beam had traveled few centimeters. The microscope objective used in this setup was designed to operate at an infinite conjugate ratio for

optimum performance. Imperfect collimation would result in the increase of the focal spot size. This increase would reduce the irradiance at the focal spot. Such a reduction would greatly affect the emission intensity since it is proportional to the square of the excitation intensity.

Similarly, the LMU objective was not optimized for 532 nm excitation and it exhibits high reflection losses at the laser wavelength of 532 nm. The objective has 6 optical elements in it. Without a coating, there will be 8% loss in intensity due to reflection per optical element. Nevertheless, the loss here may not have been up to 8% per optical element due to the fact that the optical elements were coated with anti-reflection coatings, though not at the excitation wavelength. Similarly, the objective exhibited chromatic aberration, thereby making the focal point of the excitation source on the sample to be different from that of the focal point from where the emission is collected. This difference in focal points due to chromatic aberration could have negatively affected detection limits.

Another possible problem was the fact that the entrance aperture of the objective was not fully filled because of the constraint of not making the detector very bulky. As illustrated previously, the manufacturer's specified focused spot size was 1 μm, but due to the partial filling of the entrance aperture, the calculated spot size was about 2.72 μm. This certainly reduced the irradiance at the focal spot.

In TPE, the emission intensity is proportional to the square of the excitation intensity. Therefore an increase in the excitation intensity would lead to a square increase in the emission intensity. The outlined limitations would have contributed to reduce the excitation intensity. Therefore a way to improve the detection limit would be to minimize these problems.

Similarly, the level of background signal could be significantly reduced by adding a second filter (a short pass filter) to the UG11 assuming that the background is not in the ultraviolet. However, it is likely that background is in the uv. If this is the case, there is no need to add a short pass filter. However, if the background is not in the uv, then a better filter would reduce the background emission. This would eventually result in reduced detection limits, since with efficient filtering of the background; there would no longer be a need to have a spatial filter. Ideally, TPE events are limited to the focal spot of the objective where the excitation intensity is optimum; there should be no need for a pinhole.

For the protein – BSA, the reported detection limit of 9×10^{-7} M, translates to a detection limit of 1500 molecules, assuming an excitation volume of 2.9 fL. This detection limit might look high compared to the one protein molecule detection limit reported by *Lippitz et al* [16]. However, they not only used an elaborate and expensive Ti:sapphire laser system and had a smaller excitation volume (because of the use of a high numerical aperture objective), but in addition used, a protein (hemocyanin from the tarantula

Eurypelma californicum) with 148 tryptophan residues in its amino acid sequence compared to only 3 tryptophan residues in BSA's amino acid sequence.

Ideally, one would expect that the detection limit for BSA would have been lower than the one reported here considering the number of tryptophan, tyrosine and phenylalanine residues in its amino acid sequence. There have been reports by some authors [17 – 18] that there is a significant quenching of phenylalanine and tyrosine fluorescence in proteins due primarily to energy transfer. Resonance energy transfer usually occurs when there is significant amount of overlap between the emission spectrum of one species and the excitation spectrum of the other species. Such a significant overlap does exist between phenylalanine and tyrosine and also between tyrosine and tryptophan. Similarly, the quantum yield for tryptophan in a protein is dependent on its environment. When the protein is folded, most of the tryptophan emission observed are from those residues that are exposed to the solvent [19 – 21]. This same phenomenon has been reported in proteins without tryptophan residues but with tyrosine residues [22]. Studies on protein folding, dynamics and kinetics exploit this phenomenon [23].

These two reasons and a range of other possible quenching mechanisms may have led to the decrease in tyrosine emission [24]. The ultimate result was that the detection limit for BSA was higher than what would have been expected by mere linear combination of the emission from all the tryptophans, tyrosines, and phenylalanines in the protein.

To verify that there was no significant quenching of tryptophan emission at the pH the protein and amino acids used in detection limit studies, the emission of three solutions of 0.01 M tryptophan in acetate buffer pH 5.0, water, and phosphate buffer pH 7.0 were monitored in the analog mode using the boxcar and in the digital mode using the photon counter. In all cases the signals were equal. This result was consistent with that reported in reference [17].

Tryptophan in solution was found to be more photo stable than the solid. The reason for this is probably that the molecules in solution diffuse in and out of the excitation volume.

2.6 References

1. G. Duveneck, M. Bopp, M. Ehrat, L. Balet, M. Haiml, U. Keller, G. Marowsky, and S. Soria *Two-photon fluorescence excitation of macroscopic areas on planar waveguides* Biosensors and Bioelectronics **18** (2003) 503 – 510.
2. J. Shear *Multiphoton-excited fluorescence in bioanalytical chemistry* Anal. Chem. **71** (1999) 598A – 605A.
3. A. Majewska, G. Yiu, and R. Yuste *A custom-made two-photon microscope ad deconvolution system* Pflugers Arch-Eur J Physiol **441** (2000) 398 – 408.
4. J. Ingle and S. Crouch *Spectrochemical Analysis* Prentice-Hall **1st ed** (1988) 99 – 101.
5. "Gaussian beam optics" Mells Griot
   http://www.mellsgriot.com/products/optics/gb_2.htm
   [Accessed 25 February 2004]
6. J. Amorin, and G. Baravian *The two-photon absorption laser-induced stimulated emission as a hydrogen atoms diagnostic tool: modeling and experimental* Optics Commun. **192** (2001) 227 – 286.
7. F. Jenkins and H. White *Fundamentals of optics* McGraw-Hill **4th ed** (1976) 474 – 479.
8. G. Chirico, F. Olivini, and S. Beretta *Fluorescence excitation volume in two-photon microscopy by autocorrelation spectroscopy and photon counting histogram* Appl. Specros. **54** (2000) 1084 – 1090.

9. "Schott UG11 Transmission Data Sheet" Optical Filters.com
http://www.optical-filters.com/ug11.html
[Accessed 1 March, 2004]
10. P. Schwille, U. Haupts, S. Maiti, and W. Webb *Molecular dynamics in living cells observed by fluorescence correlation spectroscopy with one-and two-photon excitation* Biophysical J. **77** (1999) 2251 – 2265.
11. A. Orden, H. Cai, P. Goodwin, and R. Keller *Efficient detection of single DNA fragments in flowing sample streams by two-photon fluorescence excitation* Anal. Chem. **71** (1999) 2108 – 2116
12. P. Dittrich, and P. Schwille *Spatial two-photon fluorescence cross-correlation spectroscopy for controlling molecular transport in microfluidic structures* Anal. Chem. **74** (2002) 4472 – 4479.
13. D. Skoog, F. Holler, and T. Nieman *Principles of instrumental analysis* **5th ed** (1998) 355 – 380.
14. "Albu_Bovin Nice Port View of Swiss Port: P02769" Expasy.org
http://us.expasy.org/cgi-bin/niceprot.pl?P02769
[Accessed 11 March 11, 2004].
15. E. Okerberg and J. Shear *Attomole-level protein fingerprinting based on intrinsic peptide fluorescence* Anal. Chem. **73** (2001) 1610 – 1613.
16. M. Lippitz, W. Erker, H. Decker, V. Holde and T. Basche *Two-photon excitation microscopy of tryptophan containing proteins* Proc. Natl. Acad. Sci. USA **99** (2002) 2772 – 2777.

17. T. Truong, R. Bersohn, P. Brumer, C. Luk and T. Tao *Effect of pH on the phosphorescence of tryptophan, tyrosine, and proteins* J. Biol. Chem. **242** (1967) 2979 – 2985.

18. J. Lakowicz *Principles of fluorescence spectroscopy*. Kluwer Academic/Plenum Publishers 2nd ed. (1999) 445 – 486.

19. B. Aruna, S. Ghosh, A. Singh, S. Mande, V. Srinivas, R. Chauhan and N. Ehtesham *Human recombinant resistin protein displays a tendency to aggregate by forming intermolecular disulfide linkages* Biochemistry **42** (2003) 10554 – 10559.

20. L.Qiu, S. Pabit, A. Roitberg and S. Hagen *Smaller and faster: the 20 –residue trp-cage protein foldes in 4 μs* J. Am. Chem. Soc. **44** (2002) 12952 – 12953.

21. C. Frieden *The kinetics of side chain stabilization during protein folding* Biochemistry **42** (2003) 12439 – 12446.

22. Y. Hitomi, C. Outten and T. Halloran *Extreme zinc-binding thermodynamics of metal sensor/regulator protein, ZntR* J. Am. Chem. Soc. **123** (2001) 8614 – 8615.

23. S. Yeh, I. Ropson and D. Rousseau *Hierarchical folding of intestinal fatty acid binding protein* Biochemistry **40** (2001) 4205 – 4210.

24. J. Lakowicz *Topics in fluorescence spectroscopy* Plenum Press **3**:Biochemical Applications (1992) 1 – 66.

Chapter 3

Excitation Volume Studies

3.1 Introduction

Accurate determination of the excitation volume was significant for proper characterization of the detector, especially as the detector was intended to be coupled to a microchip electromobility focusing (EMF) separation device. Knowing what the excitation volume was would give an idea of what the detection limits of the detector were in terms of the average number of molecules. A knowledge of the excitation volume would also guide the sizing of the EMF channel, because the separation device's detection volume window would not be less than the excitation volume of the detector, or else scatter and reflections from the channel material would interfere with the measurements. The shape of the excitation volume is shown in figure 3 – 1.

Usually, the excitation volumes in TPE detectors are in the femtoliter range. A high excitation volume would be preferred in spectroscopy as this would enhance the sensitivity of the detector because of the increased number of the analyte molecules in the excitation volume, while a smaller excitation would be preferred in microscopy to enhance its resolution. However, in TPE high excitation volumes limit the photon flux at the focal point, thereby reducing the probability of TPE excitation.

In confocal setups, the detection volume is defined in the axial direction by the waist of the excitation beam and laterally by the size of the aperture (pinhole) [1 – 2]. This

volume is dependent on the excitation beam waist at the focal point of the objective and the wavelength of excitation beam [3]. However, the challenge in accurately

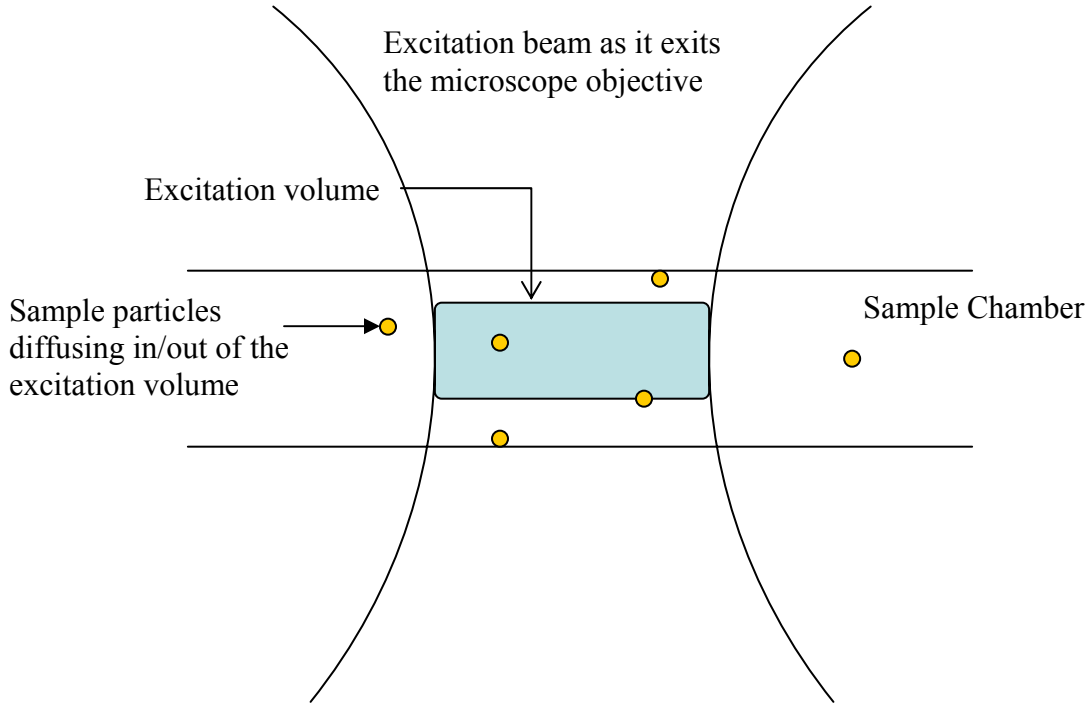

Figure 3-1. The shape of the excitation volume

determining the excitation volume lies in determining the beam waist at the objective's focal point since both the temporal and spatial profile of the excitation beam must be taken into account.

In a non-confocal TPE experiment (where a slit was used for spatial filtering), Keller et al. described an approximate method that they used to calculate the volume of the

detection region in a DNA fingerprinting detector [4]. Briefly, they assumed a cylindrical shaped radiation profile with a radius approximated by the laser waist at the $1/e^2$ value divided by $\sqrt{2}$ to account for the quadratic dependence of TPE fluorescence, while the length of the cylinder was approximated by the slit width used for spatial filtering divided by the magnification of the microscope objective.

Two complementary methods for accurate determination of detection volume have been published. Both methods are based on measuring the temporal fluctuations in the fluorescence intensity with respect to time and analyzing them either in the time or frequency domain. When the data are analyzed in the time domain, it is called fluorescence correlation spectroscopy. However, when they are analyzed in the frequency domain, the method is called photon counting histogram [5]. Also in the family of these methods is fluorescence photobleaching recovery [6].

In this chapter, discussions will be presented on the theoretical basis for these methods. A description of the experiments performed and the interpretation of the results will also be presented in this chapter.

3.2 Fluorescence Correlation Spectroscopy (FCS)

Fluorescence correlation spectroscopy is one in the family of fluctuation spectroscopic analyses. In this technique, the temporal fluctuations in fluorescence intensity from that of the excited ensembles are measured over a very short time scale and correlated with an auto correlation function. The fluctuations arise as the molecules diffuse to and from the

excitation volume. For molecules with low diffusivity, photobleaching may occur before significant data on the fluctuations is collected. In such a situation, the analytes are usually flowed through the excitation with the flow velocity incorporated into the correlation functions.

Information about the excitation volume, diffusion coefficient, chemical kinetics, aggregation, flow velocity profile can be deduced from the analysis of the magnitude and shape of the autocorrelation function [7 – 12]. However, to use this technique to measure the excitation volume, one must have knowledge of the diffusion coefficient of the molecular species used in the experiment. The fundamental theory and mathematical derivations have been given in many articles on this subject; however, I will briefly review the one given in reference 8.

Let $F(t)$ be the measured fluorescence intensity at time *t*, then the fluctuation $\delta F(t)$ from the average $\bar{F}$ resulting from a concentration $\langle C \rangle$ and volume V is given by:

$$\delta F(t) = F(t) - \bar{F} \qquad (3-1)$$

The normalized auto correlation function G(t) is given by:

$$G(\tau) = \langle \delta F(t) \delta F(t+\tau) \rangle / \langle F(t) \rangle^2 \qquad (3-2)$$

In TPE, the fluctuation could also be written as:

$$F(t) = \tfrac{1}{2} \kappa g \langle I_0(t) \rangle^2 \int_v S^2(\bar{r}) \Omega(\bar{r}) \delta(q\sigma C(\bar{r},t)).dV \qquad (3-3)$$

Where κ is the overall detection efficiency of the optical system, q is the fluorescence quantum yield of the analyte considered in the excitation volume. $\langle I_0(t) \rangle$ represent the

average intensity at the focal point and is the dimensionless spatial distribution function of the excitation beam. The square on the average intensity accounts for the quadratic dependence in TPE while the fraction accounts for the fact that the process requires the absorption of two photons. $\Omega(\bar{r})$ is another dimensionless factor and it is the collection efficiency function. When there is no spatial filtering, $\Omega(\bar{r})$ is equal to 1.

The amplitude (magnitude) of the autocorrelation function G(0) relates to the excitation volume according to the equation:

$$G(0) = V_{exc}^{-1} \langle C \rangle^{-1} \qquad (3-4)$$

So, by plotting the autocorrelation function and extrapolating to zero, the excitation volume is easily calculated from equation 3 – 4, provided the number concentration is known. In a multi-component system, the autocorrelation function is written as a summation of the contributions from each species.

The shape of the autocorrelation function can also be analyzed to determine the diffusion coefficient according to the equation:

$$G(\tau) = \frac{G(0)}{1 + (\tau / \tau_D)} \qquad (3-5)$$

Where τ_D is the diffusion time.

Hence a plot of $G^{-1}(\tau)$ as a function of τ yields a straight line with slope equal to $[\tau_D G(0)]^{-1}$ and intercept equal to $G^{-1}(0)$. From τ_D, for a TPE process, the diffusion coefficient D can be calculated from the relationship:

$$\tau_D = \omega_o^2 / (8D) \qquad (3-6)$$

Where ω_o is the excitation beam waist.

But in the case of confocal SPE case, the relationship is:

$$\tau_D = \omega_o^2 / (4D) \qquad (3-7)$$

3.3 Fluorescence Recovery after Photobleaching

Another technique that can be used to determine the excitation volume is fluorescence recovery after photobleaching. The technique can either be used to determine the diffusion coefficient of slowly diffusing molecules when the excitation beam waist is known or could be used to determine the excitation beam waist when the diffusion coefficient is known. The analysis recovers τ_D therefore based on the equation above, either the excitation beam waist or the diffusion coefficient is calculated depending on which of the two parameters was known beforehand. So, in the case of determining excitation volume, the diffusion coefficient of the molecules used in the experiment must be known, then after calculating the waist, the equation below is used to calculate the excitation volume in the case of TPE with no spatial filter [3]:

$$V_{exc} = \pi \omega_o^4 / \lambda \qquad (3-8)$$

Where λ is the excitation wavelength.

But when a spatial filter is used, then equation 3 – 9 is used to calculate the excitation volume [8]:

$$V_{exc} = \left(\frac{\pi}{2}\right)^{3/2} \omega_o^2 z_o \qquad (3-9)$$

Where z_o is the size of the spatial filter.

The technique involves irreversible photobleaching of the fluorophore by a very intense laser beam that has been tightly focused within the excitation volume. Both single photon excitation and TPE can be applied. After the bleaching process, diffusion or other transport mechanism causes unbleached molecules that were outside the excitation volume to enter the excitation volume. Fluorescence emission from these molecules entering the excitation volume is then monitored (recovery), analyzed and fitted to set of mathematical equations that have been used to model the system in order to recover τ_D [6, 13 – 17]. The derivation of these equations will not be given in this work but can be found in references 6, and 13 through 17.

3.4 Photon Counting Histogram (PCH)

This is another member of the family of fluctuation spectroscopy and was developed in 1999 by Chen and coworkers [5, 18]. An advantage of PCH over correlation spectroscopy is that the excitation volume can be determined without *a priori* knowledge of the diffusion coefficient [3]. However, the same experimental data can be used for both PCH and fluorescence correlation spectroscopy. While FCS could be said to be an analysis of fluorescence fluctuations in the time domain, PCH on the other hand is an analysis of fluorescence fluctuations in the frequency domain since it uses probability functions to analyze the fluctuations in fluorescence counts. In PCH, a histogram of the probability distribution of the photon counts detected in a time interval is plotted and fitted to a super Poisson function. The function is based on Mandel's formula of distribution of emitters with different average intensities and the knowledge of the point

spread function of the excitation beam [19]. From the shape of this distribution, information on the average number of molecules in the excitation volume and the molecular brightness are recovered. From the average number of molecules, the excitation volume can be determined based on the approach suggested by *Chirico et al*. in reference 3. The molecular brightness factor represents the average number of photons emitted by a particle in the excitation volume during the integration time and is dependent on wavelength of excitation and is proportional to the molecule's absorption spectrum [18, 20].

3.4.1 Theory

The flux of photons striking the photocathode of an optical transducer such as a photomultiplier tube or an avalanche photodiode is random. It's counting statistics were worked out by Mandel in 1959 [21 – 22] and is referred to as Mandel's formula:

$$p(k,t,T) = \int_0^\infty \frac{\left(\eta_w W(t)\right)^k}{k!} p\left(W(t)\right) dW(t) \qquad (3-10)$$

Where $p(k,t,T)$ is the probability of observing k photoelectron events at time t and integration time T. In practice, the integration time is chosen to be shorter than the fluctuation time scale of the process under study. In the case of our experiments, it has to be shorter than the diffusion time of the particles in the excitation volume. η_w is the efficiency of detection while $W(t)$ is the temporal energy profile of the excitation and $p\left(W(t)\right)$ is the energy distribution.

In shot noise limited systems, it has be shown that the photon count distribution follows a Poisson distribution [23] according to the equation:

$$Poi\left(k,\langle k\rangle\right)=\frac{(\eta_w W)^k e^{-\eta_w W}}{k!} \qquad (3-11)$$

By replacing the energy W with the intensity at the detector I_D in the Mandel's equation result's to the equation below:

$$p(k)=\int_0^\infty \frac{\left(\eta_I I_D\right)^k e^{-\eta_I I_D}}{k!} p(I_D)dI_D=\int_0^\infty Poi(k,\eta_I I_D)p(I_D)dI_D \qquad (3-12)$$

The intensity depends on the shape of the point spread function (PSF) which could be approximated by either a three dimensional Gaussian or a squared Gaussian-Lorentzian functions. Therefore, to obtain the photon counting histogram of fluorescence fluctuations, the PSF must be incorporated into the equation above.

For a squared Gaussian-Lorentzian under TPE with no spatial filter, the PCH for a single particle in a closed system to a one-dimension integral is:

$$\begin{aligned} P^{(1)}_{(2GL)}(k;V_o,\varepsilon) &= \frac{1}{V_o}\frac{\pi^2\omega_o^4}{2\lambda k!}\int_0^\infty \left(1+x^2\right)\gamma\left(k,\frac{4\varepsilon}{\pi^2\left(1+x^2\right)^2}\right)dx \\ &= \frac{1}{V_o}\frac{\pi V_{exc}}{2k!}\int_0^\infty \left(1+x^2\right)\gamma\left(k,\frac{4\varepsilon}{\pi^2\left(1+x^2\right)^2}\right)dx \end{aligned} \quad \text{for k>0.} \qquad (3-13)$$

While for a three-dimensional Gaussian also under TPE, the PCH for a one particle in a closed system to one-dimension integral is:

$$P^{(1)}_{(3dG)}(k;V_o,\varepsilon) = \frac{1}{V_o}\frac{\pi\omega_o^2 z_o}{2\cdot k!}\int_0^\infty \gamma\left(k,\varepsilon e^{-4x^2}\right)dx$$
$$= \frac{V_{exc}}{V_o}\frac{1}{k!}\left(\frac{2}{\pi}\right)^{\frac{1}{2}}\int_0^\infty \gamma\left(k,\varepsilon e^{-4x^2}\right)dx \quad \text{for k>0.} \qquad (3-14)$$

Where ε is the brightness factor, V_o is the integration volume and γ is the lower incomplete gamma function.

For N identical but independent particles, the PCH is generated by N-times self convolution of the PCH for one-particle system according to the equation:

$$p^{(N)}(k;V_o,\varepsilon) = \underbrace{\left(p^{(1)}\otimes\ldots\otimes p^{(1)}\right)}_{N-times}\left(k;V_o\varepsilon\right)$$
$$= \sum_{r_1=0}^{k}\sum_{r_2=0}^{r_1}\cdots\sum_{r_{N-1}=0}^{r_{N-2}} p^{(1)}(k-r_1;V_o,\varepsilon)p^{(1)}(r_1-r_2;V_o,\varepsilon)\cdots p^{(1)}(r_{N-2}-r_{N-1};V_o,\varepsilon)$$

……..(3 – 15)

A special case is the probability function $p^{(0)}(k;V_o,\varepsilon)$ when there is no particle in the integration volume. This probability distribution is a delta function $\delta(k)$ that is equal to 1 when the count is zero and equal to zero for counts greater than zero.

For open systems – in which the integration volume is much smaller than the volume of the reservoir, the number density of the particles through this volume will also fluctuate and would obey the Poisson distribution:

$$p_{\bar{N}}(N) = \frac{\bar{N}e^{-\bar{N}}}{N!} \qquad (3-16)$$

Where $\bar{N}$ is the average number of particles in the reference volume V_o. This average number of particles could be related to the bulk concentration c with the aid of Avogadro's number N_A as:

$$\bar{N} = cV_oN_A \qquad (3-17)$$

Hence for open systems, the PCH $\Pi(k;\bar{N},V_o,\varepsilon)$ is the average of the individual probability functions for N particles $p^{(N)}(k;V_o,\varepsilon)$ weighted by the probability of observing N particles $p_{\bar{N}}(N)$ as:

$$\Pi(k;\bar{N},V_o,\varepsilon) = \sum_{N=0}^{\infty} p^{(N)}(k;V_o,\varepsilon)\,p_{\bar{N}}(N) \qquad (3-18)$$

For multiple independent chemical species, the observed PCH is a convolution of the individual chemical species PCH. It is also worth mentioning here that the value of $\Pi(k;\bar{N},V_o,\varepsilon)$ does not depend so much on the integration volume as long as the excitation volume is equal to or greater than the integration volume [3]. In fitting the experimental photon counting histogram to the calculated histogram function, background photon counts should also be accounted for by convoluting them with $\Pi(k;\bar{N},V_o,\varepsilon)$ [3].

3.4.2 Experimental

The sample used in this study was latex spheres (40 nm diameter) labeled with neutral avidin from Floushperes, Molecular Probes. Avidin has a molecular mass of 66 kg/mol and each subunit binds to one biotin molecule. It contains four tryptophan residues.

Based on the biotin binding capacity of the spheres, the number of tryptophan residues per sphere has been calculated to be 340 [24]. The solution was diluted to particle concentrations 1.59 x 10^{-8} M and 7.97 x 10^{-9} M and was stored in the refrigerator till used.

Photon counting histogram measurements were done using the photon counter computer controlled by an in-house modified labview driver. The T counter was set to count 10 triggers corresponding to integration or sampling time of 1.5 ms. All other settings remained as described in chapter two.

After letting the laser stabilize, the flow cell was filled with the blank solution (pH 7.0 phosphate buffer) and photon counts were recorded till 10^6 data points were collected so that the resulting binomial distribution is well approximated by a normal distribution [5]. The procedure was repeated with the various concentrations of the latex spheres.

An Excel spreadsheet was used to convert the raw data into a frequency distribution which was then exported to MATHCAD where an in-house fitting program was used to fit the calculated PCH to the experimentally observed PCH based on the equations given in the previous paragraph.

3.4.3 Data Analysis

A home written MATHCAD routine (see appendix) was used to fit the observed PCH to the calculated PCH. The procedure involved first making a guess of the excitation

volume, the average number of molecules, and the brightness factor. From these values, equation 3 – 14 was solved for N = 1 for all counts greater than zero observed during the experiment. Then the probability for N = 0 was evaluated for all k that was observed experimentally. Then the probability for N = 1 was self convoluted N-times (for N = 2 to infinity) according to equation 3 – 15 for all k experimentally observed. Probability for k = 0 was obtained by normalization. Then equation 3 – 18 was solved and convoluted with the Poisson distribution of the background counts to obtain the final calculated PCH distribution. The experimental PCH $\tilde{p}(k)$ was then fitted to the calculated PCH by changing the values of the average number of molecules and brightness factor till the reduced χ^2-function below was minimized.

$$\chi^2 = \left(\frac{\sum_{k=0}^{k_{\max}} \left(M \frac{\tilde{p}(k) - \Pi(k; \bar{N}, V_o, \varepsilon}{\sigma} \right)^2}{k_{\max} - d} \right) \qquad (3 - 19)$$

Where the M is the number of samples collected and $k_{\max}$ is the maximum observed counts and d is the number of degrees of freedom given by the number of fitting parameters. The standard deviation σ is given by:

$$\sigma = \sqrt{M\tilde{p}(k)\left(1 - \tilde{p}(k)\right)} \qquad (3 - 20)$$

Then the bulk concentration was calculated using equation 3 – 17. The procedure was repeated for the various concentrations of the spheres. The calculated bulk concentration of the spheres was then plotted against the nominal bulk concentration of the spheres and

fitted to a straight line [3]. The slope of this line, represented how many times the estimated excitation volume was larger than the actual excitation.

3.4.4 Results and Discussion

Figure 3 – 2a and b shows the plots of the photon counting histogram for 7.97 x 10^{-9} M and 1.59 x 10^{-8} M latex particles respectively. The curves were fitted after convoluting an average background count of 0.17 with a 1:1 ratio between the excitation volume and the integration volume of 5.49 x 10^{-16} m^3 (assumed). From the fits, an average number of particles in the integration volume were 3.021 and 28.531 particles for the 7.97 x 10^{-9} M and 1.59 x 10^{-8} M latex particles respectively. From the average number of particles obtained from the fits and the integration volume used in the fits, the resulting concentrations were 9.13 x 10^{-12} M and 8.62 x 10^{-11} M respectively. The calculated result from the 7.97 x 10^{-9} M solution may not be reliable since the resulting brightness factor was negative. A possible reason for this could be that the concentration of tryptophan within the excitation volume was about the detection limit of the detector, which was expected theoretically.

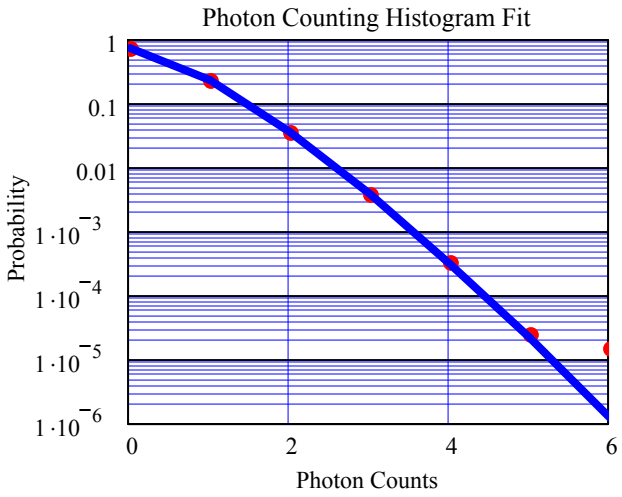

(a)

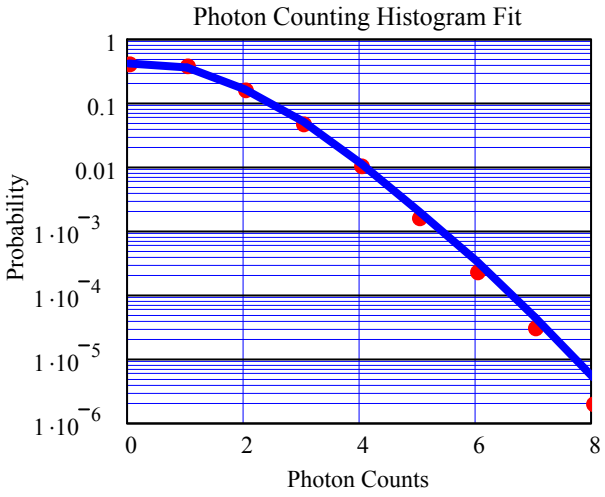

(b)

Figure 3-2. Photon counting histogram fits. (a) for 7.9 nM and (b) for 15.9 nM 0.04 micron latex spheres cross-linked with neutral avidin. The dots represent the experimentally observed probabilities while the line is the result of the fit after convoluting with a background μ_b of 0.17.

Obviously, the calculated concentrations were not equal to the nominal concentrations even for the higher concentration of particles; hence the chosen integration volume was not the right excitation volume. *Chirico et al* in reference 3 showed that there was a linear relationship between the concentrations obtained from fits and the nominal concentrations of which the slope was equal to the number of times the excitation (integration) volume was overestimated. Thus a plot of the calculated concentrations against the nominal concentrations had a slope of 0.0097 and when multiplied by the excitation volume used in the fits gives an actual excitation volume of 5.33 fL. If the calculated value from the 7.97×10^{-9} M is discarded and we use just one point, then the actual excitation volume would be 2.98 fL assuming that the slope passes through the origin.

The 2.98 fL does make sense since this was very close to the theoretically expected detection volume. However, there is a high uncertainty seeing that it was based on one concentration alone after background subtraction. Nevertheless, this value still does make sense considering the values reported by previous researchers [3, 25].

The data acquisition time was long since about 10^6 data points were required for each sample [3, 5]. It could be argued that there could have been significant photobleaching effects during the experiment. However, the result presented in chapter 2 suggested that tryptophan is relatively stable in terms of photo-degradation at the conditions that we were operating. Also, the limitation imposed by the inability of Microsoft Excel or

Mathcad to handle data points longer than 60,000 per file, caused the data acquisition to be periodically paused to enable data storage to resume on a new file. During this period, the laser shutter was closed making sure that before the next data collection cycle started, equilibrium would have been reached in the excitation volume thereby minimizing the effect of photobleaching.

Concerns about the stability of the laser intensity could also be raised since the photon detection process is sensitive to intensity fluctuations. However, because the laser was mode-locked and because the distribution of the blank followed a Poisson distribution (which was convoluted into the calculated probabilities during the fitting process), the fluctuations in laser intensity would have not significantly contributed to the outcome of the experiment.

Data obtained from this experiment could have been analyzed by correlation spectroscopy techniques as a control experiment. However, because the diffusion coefficient of the 40 nm spheres would have been hard to set, it would be difficult to recover the excitation volume from such an analysis. As such no correlation analysis was done.

3.5 References

1. M. Foquet, J. Korlach, W. Zipfel, W. Webb, and H. Craighead *Focal volume confinement by submicrometer-sized fluidic channels* Anal.Chem. **76** (2004) 1618 – 1626.
2. P. Dittrich, and P. Schwille *Spatial two-photon fluorescence cross-correlation spectroscopy for controlling molecular transport in microfluidic structures* Anal. Chem. **74** (2002) 4472 – 4479.
3. G. Chirico, F. Olivini, and S. Beretta *Fluorescence excitation volume in two-photon microscopy by autocorrelation spectroscopy and photon counting histogram* Appl. Specros. **54** (2000) 1084 – 1090
4. A. Orden, H. Cai, P. Goodwin, and R. Keller *Efficient detection of DNA fragments in flowing samle streams by two-photon fluorescence excitation* Anal. Chem. **71** (1999) 2108 – 2116.
5. Y. Chen, J. Muller, P. So, and E. Gratton *The photon counting histogram in fluorescence fluctuation spectroscopy* Boiphys J. **77** (1999) 553 – 567.
6. E. Brown, E. Wu, W. Zipfel, and W. Webb *Measurement of molecular diffusion in solution by multiphoton fluorescence photobleaching recovery* Biophys J. **77** (1999) 2837 – 2849.
7. J. Lakowicz *Topics in fluorescence spectroscopy* Plenum Press **1** (1991) 337 – 378.

8. P. Schwille, U. Haupts, S. Maiti, and W. Webb *Molecular dynamics in living cells observed by fluorescence correlation spectroscopy with one-and two-photon excitation* Biophys J. **77** (1999) 2251 – 2265.
9. S. Hess, and W. Webb *Focal volume optics and experimental artifacts in confocal fluorescence correlation spectroscopy* Biophys J. **83** (2002) 2300 – 2317.
10. E. Brown, J. Shear, S. Adams, R. Tsien, and W. Webb *Photolysis of caged calcium in femtoliter volumes using two-photon excitation* Biophys J. **76** (1999) 489 – 499.
11. H. Li, L. Ying, J. Green, S. Balasubramanian, and D. Klenerman *Ultrasensitive coincidence detection of single DNA molecules* Anal. Chem. **75** (2003) 1664 – 1670.
12. M. Gosch, H. Blom, J. Holm, T. Heino, and R. *Rifler Hydrodynamic flow profiling in microchannel structures by single molecule fluorescence correlation spectroscopy* Anal. Chem. **72** (2000) 3260 – 3265.
13. E. Keuren, and W. Schrof *Fluorescence recovery after two-photon bleaching for the study of dye diffusion in polymer systems* Macromolecules **36** (2003) 5002 – 5007.
14. O. Seksek, J. Biwersi, and A. Verkman *Translational diffusion of macromolecule-sized solutes in cytoplasm and nucleus* J. Cell Biol. **138** (1997) 131 – 142.
15. Y. Yuan, O. Velev, and A. Lenhoff Mobility of adsorbed proteins studied by fluorescence recovery after photobleaching Langmuir 19 (2003) 3705 – 3711.

16. J. Abeny, B. Cutler, M. Fillbach, D. Axelrod, and B. Scalettar *Chromatin dynamics in interphase nuclei and its implications for nuclear structure* J. Cell Biol **137** (1997) 1459 – 1468.

17. H. Munnely, D. Roess, W. Wade, and B. Barisas *Interferometric fringe fluorescence photobleaching recovery interrogates entire cell surfaces* Biophys. J. **75** (1998) 1131 – 1138.

18. G. Chirico, S. Bettati, A. Mozzarelli, Y. Chen, J. Muller, and E. Gratton *Molecular heterogeneity of o-acetyserine sulfhydrylase by two-photon excited fluorescence fluctuation spectroscopy* Biophys. J. **80** (2001) 1973 – 1985.

19. "Characterizing Si nanocrystals by FCS and PCH" University of Illunois at Urbana-Champaign
http://www.physis.uuiuc.edu/research/publications/theses/copies/akcakir/chapter4.pdf
[Accessed 23 September, 2003].

20. Y. Chen, J. Muller, Q. Ruan, and E. Gratton *Molecular brightness characterization of EGFP in vivo by fluorescence fluctuation spectroscopy* Biophys. J. **82** (2002) 133 – 144.

21. L. Mandel *Fluctuations of photon beams and their correlations* Proc. Phys. Soc. **72** (1958) 1037 – 1048.

22. L. Mandel Sub-*Poissonian photon statistics in resonance fluorescence* Optics Lett. **4** (1979) 205 – 207.

23. J. Ingle and S. Crouch *Spectrochemical Analysis* Prentice-Hall **1st ed** (1988) 99 – 101.

24. M. Lippitz, W. Erker, H. Decker, K. Holde, and T. Basche *Two-photon excitation microscopy of tryptophan-containing proteins* Pnas **99** (2002) 2772 – 2777.

25. G. Chirico, C. Fumagalli, and G. Baldini Trapped Brownian motion in single- and two-photon excitation fluorescence correlation experiments J. Phys. Chem. B 106 (2002) 2508 – 2519.

Chapter 4

Spectroscopic Characterization of Immobilized Cadmium Sensor

4.1 Introduction

The toxic and hazardous effects of cadmium (II) are well documented and it is among the thirteen heavy metal ions listed as "priority pollutants by the EPA" [1]. In humans, Cd^{2+} has been reported to cause aggravated anemia and to accumulate in organs such as spleen, kidney and thyroid gland [2 – 3]. Primary sources of environmental Cd^{2+} are phosphate fertilizers and nickel-cadmium rechargeable batteries for cellular phones and other electronic devices. Therefore, the need for fast online sensing and quantification of Cd^{2+} levels in process and waste streams and on the soil cannot be overemphasized.

Various sensing methods such as optical, electrical [4], and gravimetric methods have been used in sensing metal ions, including Cd^{2+}. Optical techniques (fluorescence) offer the highest sensitivity over the other techniques. The sensor molecule in a fluorescence based sensor can be divided into two parts – the metal ion-receptor that selectively binds to the ion and the subunit capable of signaling the occurrence of the ion-receptor interaction [5].

5-chloro-8-methoxyquinoline appended diaza-18-crown-6 **I** (figure 4–1a) is weakly fluorescent but when it complexes with Cd^{2+} its fluorescence quantum yield increases greatly as a function of Cd^{2+} concentration (see figure 4–1b) making it a promising

chemosensor for Cd^{2+} [6]. The crown ether moiety complexes the Cd^{2+} ion while the quinoline side chain acts as the signaling unit via fluorescence.

To use the above compound as a sensor, it must be mobilized on a suitable substrate that will preserve its optical activity. The work described in this chapter includes the preliminary assessment of the immobilized compound **I** on a quartz slide using polymer films via spin coating. Specific properties studied were changes in fluorescence intensity, fluorescence lifetime, photostability, and stability of the coating with and without Cd^{2+} complexation. Also described here is an online flow-through cadmium sensor based on covalently bound compound **I** on a quartz slide.

4.2 Experimental

4.2.1 Slide Immobilization and Sample Preparation

The immobilization process involved several simple coatings of a quartz slide with poly diallylldimethylammonium chloride (DADMAC), **I** and poly sodium 4-styrene sulfonate (PSS) repeated until 6 layers of polymer were obtained. The slides were prepared by A. Sathyapalan. 0.01 M solution of Cd^{2+} was prepared from $Cd(NO_3)_2$ in acetate buffer pH 5.3.

4.2.2 Experimental Setup

The experimental setup is shown in figure 4–2. An Infinity 40 – 100 (Coherent) frequency tripled Nd:YAG laser (355 nm) was passed through a beam splitter and to beam stirring prism. The front surface reflection from the prism was spatially filtered by an iris after which the resulting beam impinged on the slide which was inclined at 45^{o}.

Fluorescence was collected at 90^{o} from the front surface of the slide using two 1-inch focal length lenses and focused unto another 1mm iris or to the entrance slit of a manual scan monochromator. A 400nm to 700nm bandpass filter was inserted between the lenses to filter off scatter from the excitation, while a photomultiplier tube was used as the detector. The PMT signal was read out on a LeCroy (LT 342) digital oscilloscope triggered by the laser's Q-switch.

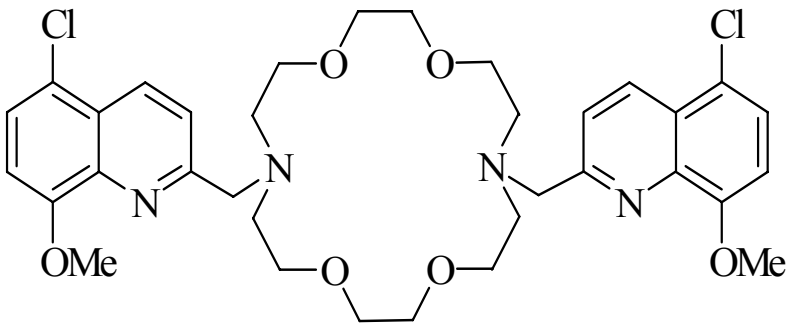

I

(a)

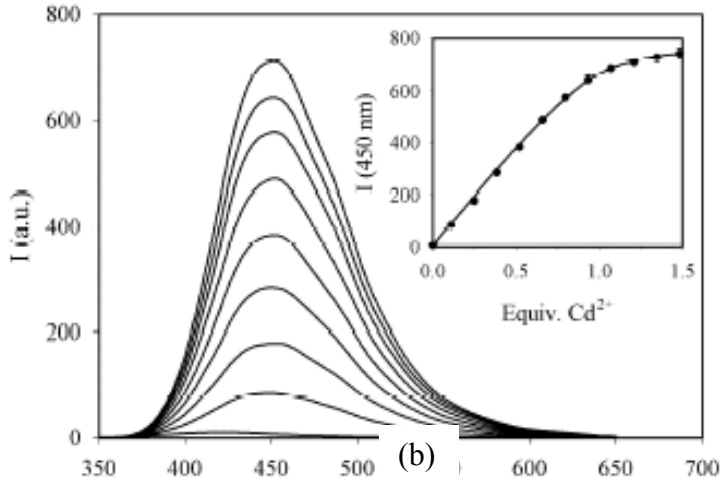

(b)

Figure 4 – 1. (a) 5-chloro-8-methoxyquinoline appended diaza-18-crown-6. This compound is weakly fluorescent but its quantum efficiency increases greatly when it complexes with Cd^{2+}. (b) Plot showing variation of fluorescence intensity of I as a function of Cd^{2+} concentration [6].

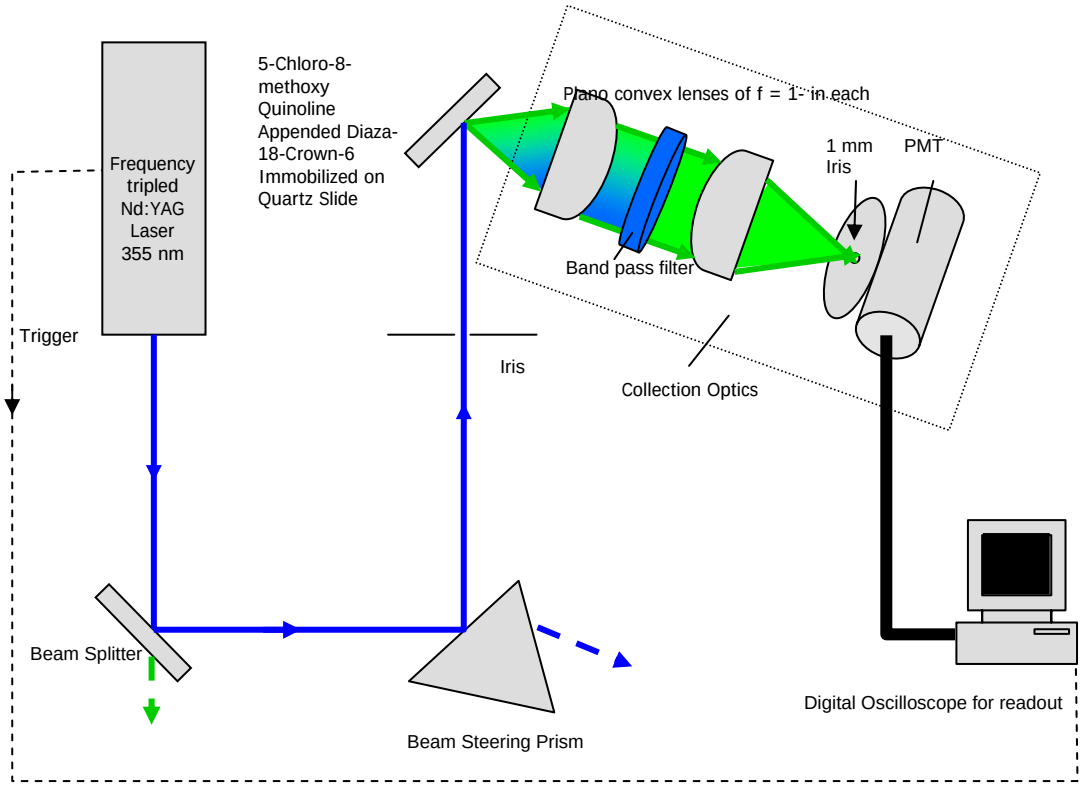

Figure 4 – 2. Experimental setup for the spectroscopic characterization of immobilized I on a quartz slide. Depending on the experiment, the collection iris was replaced with a monochromator.

4.3 Results and Discussion

Figure 4–3 shows manually scanned emission spectra of a blank slide; a slide with **I** immobilized on it; and an immobilized slide dipped in 0.01 M Cd^{2+} solution using the setup above. The result from the spectra shows the immobilization technique did not alter the spectroscopic property of **I** regarding increase in fluorescence intensity as it complexes with Cd^{2+}. In each of the spectra shown, an enhancement in signal was observed at 532 nm. This enhancement was likely due to unfiltered second harmonic frequency of the Nd:YAG which occurs at 532 nm.

In reference 6, it was shown that the fluorescence lifetime of **I** was shorter than that when it was complexed with Cd^{2+}. Figure 4–4 shows the normalized plots of the waveforms for the blank slide; slide with I immobilized and when dipped in 0.01 M Cd^{2+}. The observed decay time is a convolution of the instrument decay time and that of the compound. The de-convolution was not done and no values will be reported for the lifetimes. However, it was still evident that the lifetimes increased as the complex formed, consistent with the results published in reference 6.

The photobleaching of the immobilized I was also investigated. Figure 4 – 5 is a plot of the fluorescence intensity as a function of number of laser shots irradiated on approximately 0.785 mm^2 area with an average energy of 9 μJ at a repetition rate of 30 Hz. The result showed that after 74000 laser shots, the fluorescence intensity decreased by 21%. Therefore, the immobilized sensor molecule was relatively photo stable.

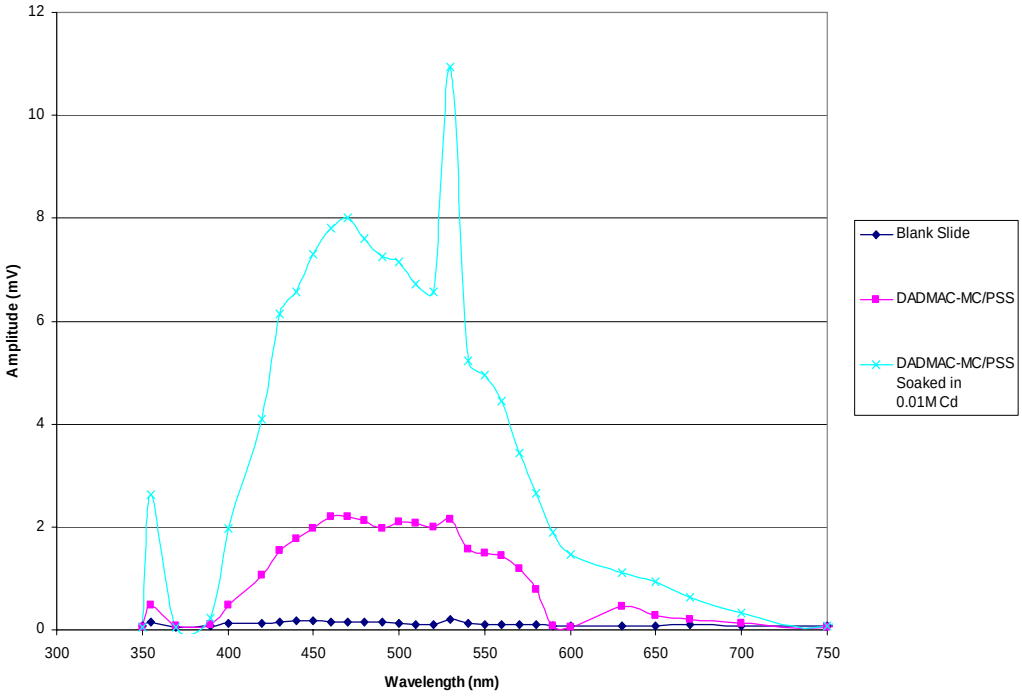

Figure 4–3. Manually obtained fluorescence emission spectra for **I** immobilized on a quartz slide, blank slide, and for **I** immobilized slide soaked in 0.01 M Cd^{2+} solution.

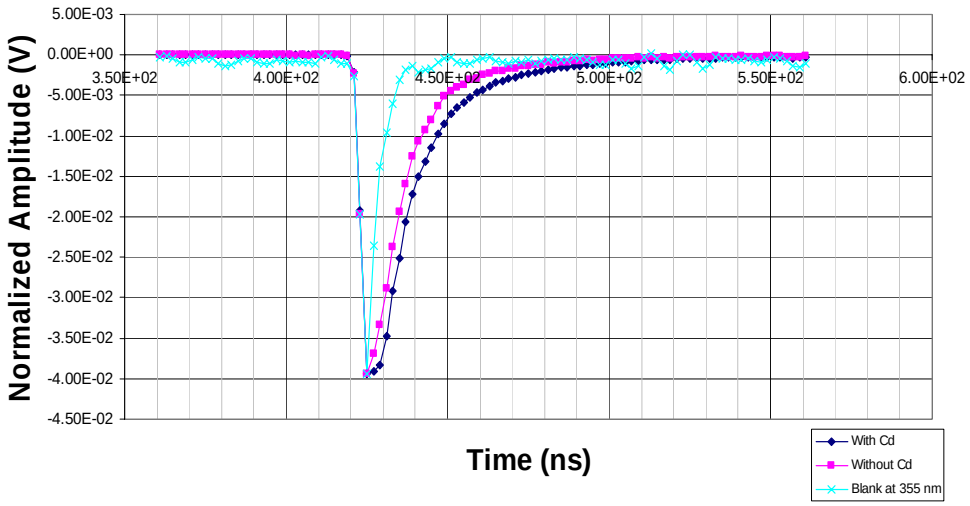

Figure 4–4. Normalized waveforms for a blank slide, slide with 5-chloro-8-methoxy quinoline appended diaza-18-crown-6 and when dipped in 0.01 M Cd^{2+}. The observed decay time in each case is a convolution of the instrument lifetime and that of the compound.

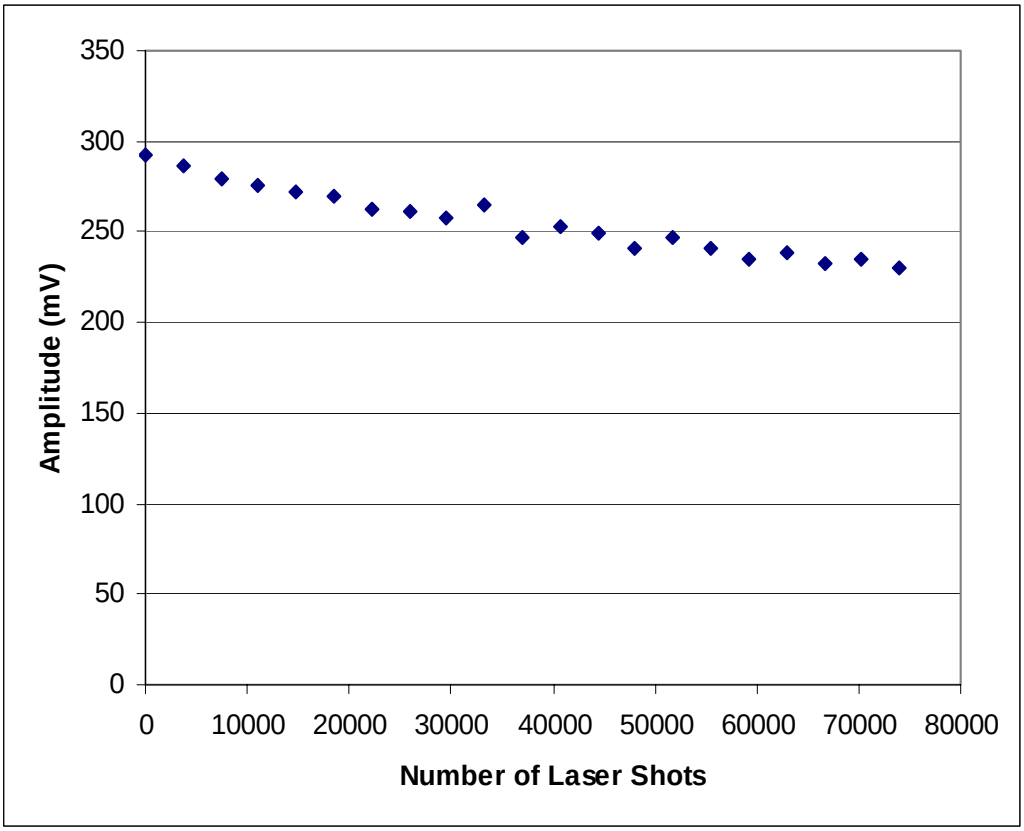

Figure 4 – 5. Photobleaching result for immobilized **I**. A 21% decrease in signal intensity was observed after 74000 laser shots on a approximate area of 0.785 mm^2. The average laser energy was 9 μJ.

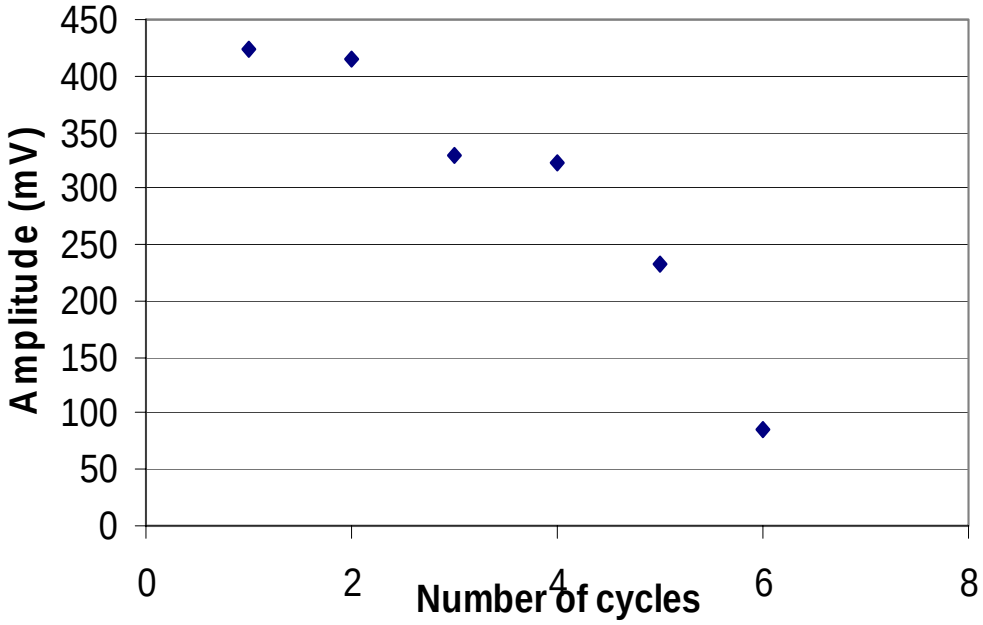

Figure 4 – 6. Cycling experiment to determine the stability of the immobilization of **I** on a slide by alternate spin coating with DADMAC/PSS. The plots represent the fluorescence signal of the immobilized **I** after the complexed Cd^{2+} had been washed off with water.

The stability of the DADMAC/PSS coating procedure used to immobilize **I** on the quartz surface was tested by repeatedly and alternately measuring the fluorescence signal as the slide was dipped in 0.01 M Cd^{2+} and then washed off with water. From figure 4 – 6, after six cycles, the signal fell by 81%. This result clearly showed that the immobilization process was not stable. Consequently, Todd Bronson developed a method to covalently bind **I** on quartz that was stable and without the loss of **I**'s spectroscopic properties [7].

The procedure involved the attachment of a $– CH_2 – O – CH_3 – CH_3NH_2$ group to one of the carbons on the crown ether that was attached to oxygen. Then the quartz slide was acid etched to form OH groups on its surface, which was consequently reacted with either amino or epoxy silane. The epoxy or amino functionalized slide was then reacted with the amine tethered **I** in the presence of THF and heat.

4.4 Design and Construction of a Field Usable Miniature Online Cadmium Sensor

The success of the covalently bound immobilization procedure described in the previous paragraph led to the design and construction of a field usable online Cadmium sensor, figure 4-7. The heart of the online sensor is a flow cell that houses the slide. The flow cell is a type 39 1-mm-path-length quartz flow cell from NSG. The flow cell consists of a top and a bottom quartz plates. The top plate has a fluid inlet and outlet connections while the bottom plate has a 1 mm deep by 10 mm wide recess housing the slide. The slide was mounted by sliding it through two rectangular Teflon blocks that had thin grooves in the middle to fit the slide. A Teflon gasket was also inserted between the top

and bottom quartz plates to ensure good sealing. The cell was finally held together by sandwiching it between two aluminum plates and was mounted on an *x*-translation stage inside the sensor box.

The excitation source was a 350 nm 40 μW @ 20 mA continuous forward current light emitting diode (LED). Because the emission from the LED was fairly broad, an optical filter was placed in its path before the light impinged on the slide. The LED was operated in 10% duty cycle pulse mode for optimum power since the forward current could be increased to as high as 100 mA. Emission from the LED was broad and overlapped with the emission spectrum of **I**. Therefore, a DAPI exciter and emitter filter set from Semrock was used to block the LED emission from being collected and reaching the photomultiplier tube. A pair of lenses was used to collimate and focus the LED onto the slide, while another pair of lenses was used to collect the emission and focus it unto a 1 mm iris.

The excitation was introduced at the Brewster's angle for glass ($58^{o}40'$) to reduce the reflection of the excitation beam, since the reflectance of the parallel component of light is zero at the Brewster's angle [8]. The emission was collected perpendicular to the flow cell. The photomultiplier tube output was connected to a lock-in analyzer (Princeton Applied Research model 5204). The 10% duty cycle square wave used to trigger the LED power supply was also used as the reference frequency for the lock-in analyzer. The lock-in output was connected to the computer and data was acquired using a National

Instrument Virtual Bench Logger. Figure 4 – 7 shows the schematic diagram of the sensor.

The sensor's figures of merit are yet to be characterized but it is hoped that the sensitivity and detection limits will be fairly good and comparable to similar techniques.

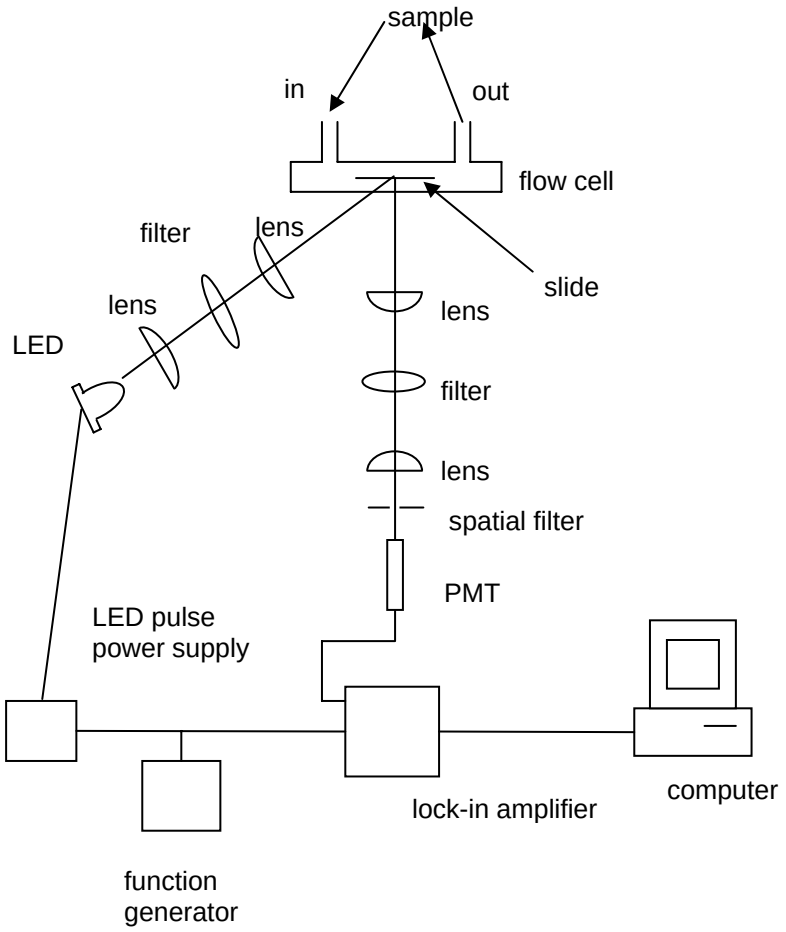

Figure 4 – 7. Optical and instrumental setup of a field usable online cadmium sensor based on covalently immobilized 5-choloro-8-methoxyquinoline appended diaza-18-crown-6 on a quartz slide. The covalent immobilization and characterization of the compound on the slide was done by T. Bronson [7].

4.5 References

1. Y. Zhang, C. Murphy, and W. Jones *Poly[p-(phenyleneethynylene)-alt-(thienyleneethynylene)] polymers with oligopyridine pendant groups: highly sensitive chemosensors for transition metal ions* Macromolecules **35** (2002) 630 – 636.
2. Y. Chun, E. Choi, G. Kim, H. Choi, C. Kim, M. Lee, M. Kim, and J. Park *Cadmium blocks hypoxia-inducible factor (HIF)-1-mediated response to hypoxia by stimulating the proteasome-dependent degradation of HIF-1α* Eur. J. Biochem. **267** (2000) 4198 – 4204.
3. T. Gunnlaugsson, C. Lee, and R. Parkesh *Cd(II) sensing in water using novel aromatic iminodiacetate based fluorescent chemosensors* Org. Lett. **5** (2003) 4065 – 4068.
4. M. Pineros, J. Shaff, and L. *Kochian Development, characterization, and application of a cadmium-selective microelectrode for the measurement of cadmium fluxes in roots of thlaspi species and wheat* Plant Physiol. **116** (1998) 1393 – 1401.
5. J. Kawakami, R. Miyamoto, K. Kimura, K. Obata, M. Nagaki, and H. Kitahara J. Comput. Chem. Jpn. 2 (2003) 57 – 62.
6. L. Prodi, M. Montalti, N. Zaccheroni, J. Bradshaw, R. Izatt, and P. Savage *Characterization of 5-methoxyquinoline appended diaza-18-crown-6 as a chemosensor for cadmium* Tetrahedron Lett. **42** (2001) 2941 – 2944.
7. T. Bronson *Molecular chemosensors for heavy metals: from synthesis to reusable device* PhD Dissertation (2003) 77 – 96.

8. J. Ingle and S. Crouch *Spectrochemical analysis* Prentice Hall **1st ed** (1998) 30 – 86.

Chapter 5

Summary and Future Directions

A relatively inexpensive two-photon excitation fluorescence detector for proteins was built and characterized. Though the figures of merit for this detector are promising, with a potential of coupling it to a microchip separation device, more work is needed to fully optimize the system. Also characterized was immobilized 5-chloro-8-methoxyquinoline appended-diaza-18-crown-6 on quartz as a sensor for cadmium which led to the design and construction of a field usable online cadmium sensor. The results presented in the previous chapters will be summarized in this chapter. Recommendations for future study will be given thereafter.

5.1 Summary of Results

5.1.1 Two-Photon Excitation Protein Fluorescence Detector Design

Three important features set the detector described in this report apart from the others of its kind. The three features are that it was relatively inexpensive, compact because of the use of a diode pumped microchip laser for the excitation source as against the use of the bulky and very expensive femtosecond Ti:Sapphire laser, and affords longer working distance [1 – 10]. The detector's detection limits for the three aromatic amino acids were 4 μM for tryptophan, 22.5 μM for tyrosine, and 500 μM for phenylalanine. For the protein bovine serum albumin, the detection limit was 0.9 μM. The detection limits for individual proteins vary and depend on how many of the aromatic amino acid residues in its sequence. With the excitation volume calculated to be 2.98 fL, the detection limits

cited above were below the atto-mole range. These detection limits for this detector however, were about an order of magnitude higher than the ones reported with the use of more elaborate laser systems. Some likely reasons for such a higher detection limit are discussed in chapter 2, such as the inability to fully fill the microscope objective and reflection losses at the surfaces of the optical elements in the objective. Another factor is the high background level that prompted the use of a spatial filter. Therefore, more analysis of the background is needed so as to effectively minimize it without attenuating the signal greatly.

5.1.2 Immobilized Cadmium Chemosensor Characterization

The characterization of immobilized chemosensor showed that 5-chloro-8-methoxyquinoline appended-diaza-18-crown-6 [11] retained its spectrochemical properties when immobilized on a quartz slide and was even very stable when the compound was covalently attached [12] making it seem promising to be used as an online cadmium sensor. A field usable online cadmium sensor that will use 5-chloro-8-methoxyquinoline appended-diaza-18-crown-6 covalently attached on a quartz slide as the active sensing medium was designed and fabricated.

5.2 Recommendations for Future Study

5.2.1 Two-Photon Excitation Fluorescence Protein Detector

The protein detector described in this work surely is not fully optimized. However, from the characterization studies, insights were derived on perhaps things that could be done to further optimize the detector and lower its detection limits. Studies on how to efficiently

reduce the divergence of the laser beam without an appreciable increase in the overall size of the detector would be helpful in optimizing the detector's performance. Perhaps, the incorporation of an off-axis concave mirror before the beam expander might be helpful.

Similarly, further studies should be done on background characterization. The understanding of the spectral distribution of the background would help in proper identification of its source and how to effectively reduce it without attenuating the analytical signal. By reducing the background to the barest minimum, there will no longer be the need for a spatial filter.

Furthermore, because microchip channels are in very small dimensions, it is critical to make sure that the focal plane of the objective is located within the channel space. This would require tedious alignment and a steady sample holder. However, if an ocular piece is added to the present design, it will enable the visual alignment which is simpler. In fact a design to accommodate this feature had already been made and most of the parts have also been ordered.

5.2.2 Online Cadmium Sensor

The online cadmium was not characterized. It will be important to carryout a full characterization of the sensor to determine what its detection limits are, and also its selectivity with respect to other interfering ions. This might lead to the incorporation of a sample pretreatment stage before the sample actually comes in contact with the

immobilized slide. Time-resolved fluorescence may also be studied to see how it can be used to minimize perhaps interferences from other ions. Similarly, the use of a monochromatic excitation source, such as a compact 355 nm diode pumped microchip laser would perhaps increase the sensitivity of the sensor.

5.3 Final Summary

A 532 nm diode pumped microchip nano laser was used to build a two-photon excitation fluorescence detector for proteins based on protein's intrinsic fluorescence. The detector was of average sensitivity and could easily be coupled to a microchip separation device for proteins (without labeling), peptides, and aromatic amino acids. It could also be used to study protein folding and other protein-protein interactions. The major figures of merit of this detector; when compared to others of its kind are that it is relatively inexpensive and also compact.

Similarly, 5-chloro-8-methoxyquinoline appended-diaza-18-crown-6 seems promising as a cadmium chemosensor. The compound is weakly fluorescent, but when it is complexed with cadmium exhibits an increase in fluorescence quantum efficiency. Immobilization did not destroy its spectroscopic properties, as such an online field usable cadmium sensor was designed and constructed based on covalently attached chemosensor on a quartz slide.

5.4 References

1. E. Okerberg and J. Shear *Attomole-level protein fingerprinting based on intrinsic peptide fluorescence* Anal. Chem. **73** (2001) 1610 – 1613
2. M. Foquet, J. Korlach, W. Zipfel, W. Webb, and H. Craighead *Focal volume confinement by submicrometer-sized fluidic channels* Anal.Chem. **76** (2004) 1618 – 1626.
3. P. Dittrich, and P. Schwille *Spatial two-photon fluorescence cross-correlation spectroscopy for controlling molecular transport in microfluidic structures* Anal. Chem. **74** (2002) 4472 – 4479.
4. G. Chirico, F. Olivini, and S. Beretta *Fluorescence excitation volume in two-photon microscopy by autocorrelation spectroscopy and photon counting histogram* Appl. Specros. **54** (2000) 1084 – 1090
5. A. Orden, H. Cai, P. Goodwin, and R. Keller *Efficient detection of DNA fragments in flowing samle streams by two-photon fluorescence excitation* Anal. Chem. **71** (1999) 2108 – 2116.
6. Y. Chen, J. Muller, P. So, and E. Gratton *The photon counting histogram in fluorescence fluctuation spectroscopy* Boiphys J. **77** (1999) 553 – 567.
7. G. Duveneck, M. Bopp, M. Ehrat, L. Balet, M. Haiml, U. Keller, G. Marowsky, and S. Soria *Two-photon fluorescence excitation of macroscopic areas on planar waveguides* Biosensors and Bioelectronics **18** (2003) 503 – 510.
8. J. Shear *Multiphoton-excited fluorescence in bioanalytical chemistry* Anal. Chem. **71** (1999) 598A – 605A.

9. A. Majewska, G. Yiu, and R. Yuste *A custom-made two-photon microscope ad deconvolution system* Pflugers Arch-Eur J Physiol **441** (2000) 398 – 408.
10. M. Lippitz, W. Erker, H. Decker, V. Holde and T. Basche *Two-photon excitation microscopy of tryptophan containing proteins* Proc. Natl. Acad. Sci. USA **99** (2002) 2772 – 2777.
11. L. Prodi, M. Montalti, N. Zaccheroni, J. Bradshaw, R. Izatt, and P. Savage *Characterization of 5-methoxyquinoline appended diaza-18-crown-6 as a chemosensor for cadmium* Tetrahedron Lett. **42** (2001) 2941 – 2944.
12. T. Bronson *Molecular chemosensors for heavy metals: from synthesis to reusable device* PhD Dissertation (2003) 77 – 96.

Appendix

MATCAD Curve fitting routine for fitting experimental photon counting histogram data to photon counting histogram equations developed by Yan Chen et al Biophys. J. **77** (1999) 553 – 567.

Enter the wavelength and numerical aperture of the microscope objective:

$\lambda :=$ ▮ NA := ▮

The beam waist is:

$\omega := 0.61 \cdot \frac{\lambda}{NA}$ $\omega =$ ▮

Enter the size of the pinhole in meters

$z := 150 \cdot 10^{-6}$

Guessed Volume of Exictation is:

$Vexc := \left(\frac{\pi}{2}\right)^{\frac{3}{2}} \cdot \omega^2 \cdot z$ Vexc = ▮

Enter how many times 'x' of the excitation volume you want the integration volume to be. Note that 'x' must be <= 1.

x := 1

Vo := x·Vexc Vo = ▮

Enter the maximum counts 'kmax' observed in the experiment. The program assumes that the minium count is zero. Also enter the number of data points 'MP' collected in the experiment.

kmax:= ▮ MP := ▮

Enter guess values for the average number of molecules 'D' and the brightness 'a'

D := ▮ a := ▮

Enter the background noise μ_b in the system. Also enter the observed histogram probabilities as 'PO' a function of counts k. Enter the data as a matrix of one column and kmax+1 rows.

μb := PO :=

Scroll to the last page to view results

tt := $\mu b^{0.5}$

N := 150

```
IT ( a , D ) :=
  V ← Vexc
  B ← Vo
  P ← | for k ∈ 1 .. kmax
      |   PT k − 1 ← ( V · ( 2 / π )^(1/2) / ( B · k ! ) ) · ∫_0^∞ ( ∫_0^(a · exp(−4 · x^2)) t^(k − 1) · exp(−t) dt ) dx
      | PT
  count0 ← 1 − Σ P
  I ← | for i ∈ 0 .. kmax
      |   m i ← 1 if i = 0
      |   m i ← 0 otherwise
      | m
  X ← stack ( count0 , P )
  U ← | R ← X
      | for n ∈ 0 .. N
      |   for k ∈ 0 .. kmax
      |     for j ∈ 0
      |       sum ← 0
      |       for r ∈ 0 .. k
      |         m ← k − r
      |         sum ← sum + R m , n · R r , 0
      |       Y k , j ← sum
      |     A ← augment ( R , Y )
      |     R ← A
      | R
  H ← augment ( I , U )
  L ← | for k ∈ 0 .. kmax
      |   sum ← 0
      |   for n ∈ 0 .. N + 1
      |     sum ← sum + H k , n · D^n · exp(−D) / n !
      |   prob k ← sum
      | prob
  Z ← | for k ∈ 0 .. kmax
      |   Y k ← ( tt^k · exp(−tt) / k ! )
      | Y
  W ← | for o ∈ 0 .. kmax
      |   sum1 ← 0
      |   for rr ∈ 0 .. o
      |     mm ← o − rr
      |     sum1 ← sum1 + L mm · Z rr
      |   G o ← sum1
      | G
  σ ← | for jj ∈ 0 .. kmax
      |   DD jj ← [ MP · PO jj · ( 1 − PO jj ) ]^0.5
      | DD
  χ 2 ← | chi2 ← 0
        | for kk ∈ 0 .. kmax
        |   chi2 ← chi2 + [ MP · ( PO kk − W kk ) / σ kk ]^2
        | chi22 ← chi2 / ( kmax − 2 )
        | χ 2
```

Evaluate $P^{(1)}$ (k>=1)

Evaluate $P^{(1)}$(k=0) by normalization

Calculate $P^{(0)}$

Stack $P^{(1)}$(k=0) with $P^{(1)}$(k>=1)

Generate $P^{(N)}$ for all N>=2 by self-convoluting $P^{(1)}$ N times

Calculate Π(k;a,Vo)

Calculate Poi(k,μ_b) where μ_b = tt is the background noise.

Convolute P(k) with Poi(k,μ_b)

Calculate σ(k)

Calculate the χ^2.

$$\begin{pmatrix} a \\ D \end{pmatrix} := \text{Minimize}(HT, a, D)$$

Minimize the χ^2 by changing the guessed values of a and D

The brightness is $a =$

The average number of molecules is $D =$

$PC(a, D) :=$

$V \leftarrow Vexc$

$B \leftarrow Vo$

$P \leftarrow$ for $k \in 1..kmax$

$$PT_{k-1} \leftarrow \frac{V \cdot \left(\frac{2}{\pi}\right)^{\frac{1}{2}}}{B \cdot k!} \cdot \int_0^{\infty} \left(\int_0^{a \cdot \exp\left(-4 \cdot x^2\right)} t^{k-1} \cdot \exp(-t)\, dt \right) dx$$

PT

$count0 \leftarrow 1 - \sum P$

$I \leftarrow$ for $i \in 0..kmax$

$m_i \leftarrow 1$ if $i = 0$

$m_i \leftarrow 0$ otherwise

m

$X \leftarrow stack(count0, P)$

$U \leftarrow R \leftarrow X$

for $n \in 0..N$

for $k \in 0..kmax$

for $j \in 0$

$sum \leftarrow 0$

for $r \in 0..k$

$m \leftarrow k - r$

$sum \leftarrow sum + R_{m,n} \cdot R_{r,0}$

$Y_{k,j} \leftarrow sum$

$A \leftarrow augment(R, Y)$

$R \leftarrow A$

R

$H \leftarrow augment(I, U)$

$L \leftarrow$ for $k \in 0..kmax$

$sum \leftarrow 0$

for $n \in 0..N + 1$

$$sum \leftarrow sum + H_{k,n} \cdot D^n \cdot \frac{\exp(-D)}{n!}$$

$prob_k \leftarrow sum$

$prob$

$Z \leftarrow$ for $k \in 0..kmax$

$$Y_k \leftarrow \left(tt^k \cdot \frac{\exp(-tt)}{k!} \right)$$

Y

$W \leftarrow$ for $o \in 0..kmax$

$sum1 \leftarrow 0$

for $rr \in 0..o$

$mm \leftarrow o - rr$

$sum1 \leftarrow sum1 + L_{mm} \cdot Z_{rr}$

$G_o \leftarrow sum1$

G

W

Use the new values of a and D to recalculate Π

$\Pi := PC(a, D)$

Generate the column vector k for the x-axis

$$K := \left| \begin{array}{l} \text{for } i \in 0..kmax \\ \quad KK_i \leftarrow i \\ KK \end{array} \right.$$

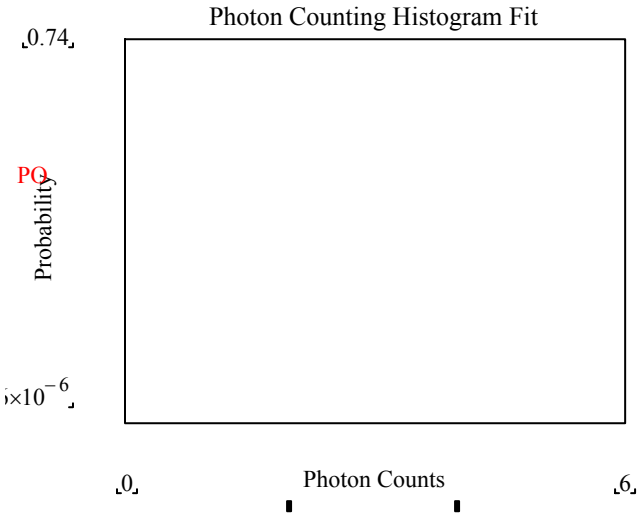

Plot the new □ and PO against k

The brightness factor is a = ▮

The average number of molecules is D = ▮